

Learning Adaptive Fusion Bank for Multi-modal Salient Object Detection

Kunpeng Wang^{1b}, Zhengzheng Tu^{1b}, Chenglong Li^{1b}, Cheng Zhang, Bin Luo^{1b}, *Senior Member, IEEE*

Abstract—Multi-modal salient object detection (MSOD) aims to boost saliency detection performance by integrating visible sources with depth or thermal infrared ones. Existing methods generally design different fusion schemes to handle certain issues or challenges. Although these fusion schemes are effective at addressing specific issues or challenges, they may struggle to handle multiple complex challenges simultaneously. To solve this problem, we propose a novel adaptive fusion bank that makes full use of the complementary benefits from a set of basic fusion schemes to handle different challenges simultaneously for robust MSOD. We focus on handling five major challenges in MSOD, namely center bias, scale variation, image clutter, low illumination, and thermal crossover or depth ambiguity. The fusion bank proposed consists of five representative fusion schemes, which are specifically designed based on the characteristics of each challenge, respectively. The bank is scalable, and more fusion schemes could be incorporated into the bank for more challenges. To adaptively select the appropriate fusion scheme for multi-modal input, we introduce an adaptive ensemble module that forms the adaptive fusion bank, which is embedded into hierarchical layers for sufficient fusion of different source data. Moreover, we design an indirect interactive guidance module to accurately detect salient hollow objects via the skip integration of high-level semantic information and low-level spatial details. Extensive experiments on three RGBT datasets and seven RGBD datasets demonstrate that the proposed method achieves the outstanding performance compared to the state-of-the-art methods. The code and results are available at <https://github.com/Angknpng/LAFB>.

Index Terms—Salient object detection (SOD), adaptive fusion bank, indirect interactive guidance.

I. INTRODUCTION

THE purpose of salient object detection (SOD) is to detect and segment the most prominent region in a given visible image. Due to the practicality of SOD in image processing, it has become an auxiliary tool for many

This work was supported in part by the National Natural Science Foundation of China under Grant 62376005, 61876002, in part by the Natural Science Foundation of Anhui Higher Education Institution of China under Grant KJ2020A0033, in part by Anhui Provincial Natural Science Foundation under Grant 2108085MF211, in part by Anhui Energy Internet Joint Fund Project under Grant 2008085UD07, in part by Anhui Provincial Key Research and Development Program under Grant 202104d07020008. (Corresponding author is Bin Luo)

Kunpeng Wang, Zhengzheng Tu, Cheng Zhang and Bin Luo are with Information Materials and Intelligent Sensing Laboratory of Anhui Province, Anhui Provincial Key Laboratory of Multimodal Cognitive Computation, School of Computer Science and Technology, Anhui University, Hefei 230601, China (e-mail: kp.wang@foxmail.com; zhengzhengahu@163.com; cheng.zhang@ahu.edu.cn and luobin@ahu.edu.cn)

Chenglong Li is with Anhui Provincial Key Laboratory of Multimodal Cognitive Computation, School of Artificial Intelligence, Anhui University, Hefei 230601, China, and also with the Institute of Physical Science and Information Technology, Anhui University, Hefei 230601, China (e-mail: lcl1314@foxmail.com)

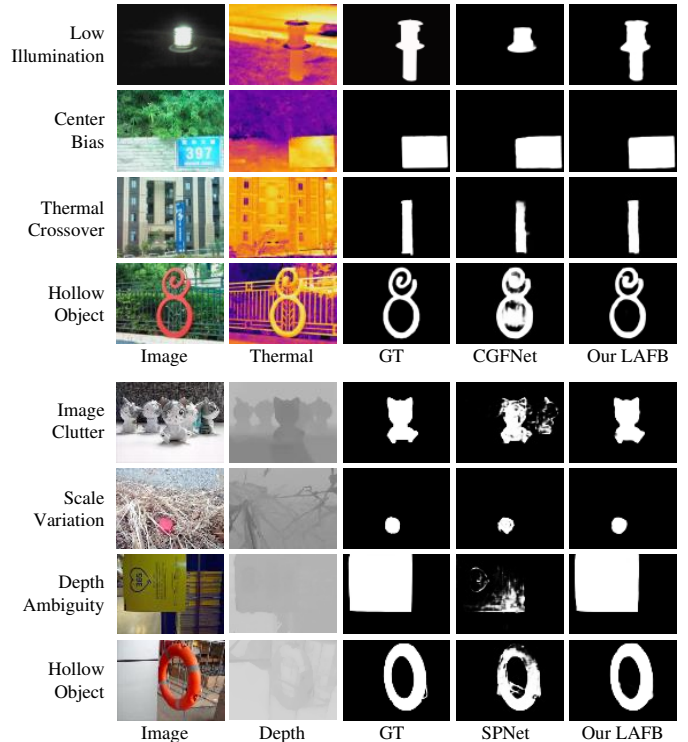


Fig. 1. **Top:** Comparison of our LAFB against a state-of-the-art RGBT SOD method, e.g., CGFNet [1]. **Bottom:** Comparison of our LAFB against a state-of-the-art RGBD SOD method, e.g., SPNet [2]. The results show that our LAFB can simultaneously handle both modality-shared challenges (i.e., center bias, scale variation, and image clutter) and modality-specific challenges (i.e., low illumination, thermal crossover or depth ambiguity), as well as accurately segment hollow objects. The compared methods can only tackle the certain challenge. For example, CGFNet can handle the center bias challenge well but fails on the low illumination and thermal crossover challenges, and SPNet can handle the scale variation challenge well but fails on the image clutter and depth ambiguity challenges. Neither of them can cope with the hollow objects.

computer vision applications, such as video segmentation [3], semantic segmentation [4], and cropping [5]. Most of SOD methods [6]–[9] are based only on RGB images and achieve remarkable results. However, these RGB-based SOD methods may struggle to segment salient objects from background in complex scenes, such as those with low illumination or similar foreground and background. To overcome the limitations of the RGB modality, depth maps and thermal infrared images are introduced to provide complementary information for multi-modal salient object detection (MSOD), including RGB-Depth (RGBD) SOD and RGB-Thermal (RGBT) SOD.

Traditional MSOD methods [10]–[12] rely on manual

features or heuristic priors to predict salient regions and outperform RGB-based SOD methods. However, they do not sufficiently explore the complementarity of multi-modal features or capture enough semantic information. Recently, many convolutional neural network-based methods [13]–[17] are proposed to fully integrate multi-modal and multi-level features for accurate detection. Nevertheless, two key issues in MSOD remain to be addressed. (1) Existing multi-modal SOD methods [14], [18]–[21] mainly design different fusion strategies to exploit the complementary information between the modalities. Despite the performance improvement gained over RGB-based SOD methods, they still fail in some challenging scenarios, such as those with depth ambiguity, thermal crossover, low illumination, image clutter, etc. Some methods [1], [22], [22]–[27] are recently proposed to address specific challenges, such as depth ambiguity [22], [24]–[27] and low illumination [1], [22], [23]. However, these fusion strategies aim to address certain challenges rather than addressing multiple challenges at the same time. As shown in the upper three rows of both RGBT and RGBD cases in Fig. 1, while the compared methods handle the center bias or scale variation challenges well, they fail in other main challenges. (2) Multi-level fusion is widely used in multi-modal SOD methods [1], [2], [28]–[33] to segment foreground from background distinctly by integrating high-level semantic features and low-level detailed features. The most common approach is top-down fusion, which directly combines the features of adjacent layers through concatenation, summation [1], [29], [31] or an integration module [2], [30]. Due to the limited number of adjacent layers, these methods restrict the feature variety and prevent the full fusion of high-level and low-level features. To address this limitation, some other methods [28], [33] integrate multi-level features directly before top-down fusion to learn richer feature representations for each layer. However, these methods may overlook the unique characteristics of the features in different layers, limiting the exploration of complementarity between high-level and low-level features. Moreover, direct integration of multi-level features may compromise the original information in these features. Therefore, fully integrating multi-level features remains a key issue in MSOD. In complex scenes with hollow objects, such as those illustrated in the last row of both RGBT and RGBD cases in Fig. 1, foreground and background are intertwined, making it difficult to accurately separate salient objects from the background. The compared methods [1], [2] struggle to distinguish the background inside the hollow object and misjudge non-salient regions as salient regions. This is mainly because they fail to fully aggregate semantic and detailed information.

To address these issues, we propose to learn an adaptive fusion bank (LAFB) for MSOD. To tackle the first issue, we design an adaptive fusion bank that consists of five representative fusion schemes and an adaptive ensemble module. The fusion schemes are separately designed according to the characteristics of the five major challenges in MSOD, namely center bias, scale variation, image clutter, low illumination, and thermal crossover or depth ambiguity. By embedding them into the encoder, the features extracted by the backbone

can be decoupled into multiple specific features that deal with different challenges. The fusion schemes are simple but effective, and each of them only needs to learn a few parameters for a specific challenge and has less dependence on data. Additionally, the adaptive ensemble module takes the feature maps generated by different fusion schemes as input and learns their weights for adaptive fusion. In this way, our adaptive fusion bank can select the corresponding fusion schemes based on the challenges in different input data. Although the adaptive ensemble module is inspired by channel attention mechanism [34], [35], their impact is completely different. Channel attention mainly focuses on refining feature representations by modeling the channel dependencies of independent features, while our adaptive ensemble module is responsible for adaptively integrating features that can deal with different challenges with different weights. In this way, the parameters of each fusion scheme can be trained accordingly. As shown in Fig. 1, our method can better handle multiple complex challenges simultaneously due to the benefits from the adaptive fusion bank. It is also worth noting that the bank is scalable and can incorporate more fusion schemes to deal with more challenges. In the future work, we will also introduce a common fusion scheme for the remaining challenges in MSOD.

For the second issue, we design an indirect interactive guidance module (IIGM) which takes into account the unique characteristics of multi-level features to achieve full and smooth integration. Considering direct integration may prevent the full integration of high-level and low-level features, we group the features of three adjacent layers and use the middle-level features as a medium to indirectly interact the high-level and low-level features. As the shown in the saliency maps in the last row of Fig. 1, the features through our IIGM can accurately segment the salient regions of hollow objects. To sum up, our contributions are as follows:

- We propose a novel adaptive fusion bank (AFB) to handle multiple complex challenges in MSOD simultaneously. The AFB takes full advantage of the complementary benefits of different fusion schemes and integrates them via an adaptive ensemble module. The bank is scalable, and more fusion schemes can be incorporated to address additional challenges.
- We design an indirect interactive guidance module (IIGM) to effectively integrate high-level semantic features and low-level detailed features, allowing for precise segmentation of salient regions of hollow objects.
- Extensive experiments on seven RGBD SOD datasets and three RGBT SOD datasets as well as ablation studies demonstrate the effectiveness of our method and each component.

II. RELATED WORK

A. RGBT Salient Object Detection

RGBT salient object detection (SOD) aims to detect common salient objects from RGB and thermal image pairs. Traditional methods often use manual features [10] or heuristic priors [11], [12] to discover complementary information

between modalities. While these have improved performance, they often fail to extract semantic information, making them less effective at dealing with complex challenges such as image cluster and low illumination.

As convolutional neural network illustrates superior feature extraction ability, a large number of methods with different fusion modules have been proposed to address corresponding issues, such as modality complementarity [13], [19], [36] and misalignment [37]. Zhang et al. [13] treat RGBT saliency detection as a feature fusion problem and propose a multi-modal fusion module to fully exploit the complementarity between RGB and thermal features. Tu et al. [36] integrate local detail information, global context, and multi-modal features to model multiple interactions between two modalities. Huo et al. [19] propose a lightweight fusion module that efficiently integrates multi-modal features by exploiting the characteristics of two modalities. For unaligned RGBT image pairs, DCNet [37] establishes strong modality correlations through multi-branch affine transformations. However, due to the lack of the design specific for challenges, these methods might fail when facing challenging scenarios.

Besides, some other methods are proposed to improve detection performance in challenging scenarios, such as low illumination [1], [22], [23] and thermal crossover [22]. Wang et al. [1] fully integrate cross-modal information through mutual guidance between RGB and thermal modalities to improve performance in low illumination. ECFNet [23] designs a bilateral fusion of foreground and background information to extract complete boundaries, and then embeds them into multi-level features for accurate detection in low-light conditions. CCFNet [22] embeds cross-modal fusion into the encoder to discriminatively extract features in the case of modality defects.

Although these studies are proposed for specific challenges, they might not cover multiple major challenges. To effectively deal with specific issues or challenges, the fusion schemes in the above methods are complex and involve a lot of parameters. However, due to the limited amount of multi-modal data, it is difficult to train these fusion schemes to learn a large number of parameters for multiple challenges. Instead, they may only be effective when learning a relatively small number of parameters for specific challenges. In our paper, we design different fusion schemes according to the characteristics of each challenge, which have simple and basic structures. By decoupling the extracted features for different challenges, each fusion scheme only needs to learn a few parameters for a specific challenge and has less dependence on data.

B. RGBD Salient Object Detection

RGBD SOD methods typically use depth maps as supplementary information to enhance RGB modality. Several deep learning-based methods are proposed to explore the sufficient fusion of cross-modal complementarity [2], [20], [38]–[40]. For example, Qu et al. [20] design handcrafted features from input images and feed them into the convolutional neural network stream for saliency guidance. Chen et al. [38] design a three-stream network to enhance the representation of multi-modal features. Fu et al. [39] fuse multi-modal features

through a Siamese network to explore representative saliency features in the feature extraction phase. Liu et al. [40] design a selective self-mutual attention that selectively supplements complementary information based on the information of the other modality. SPNet [2] captures specific and shared features through a modality-specific branch and a modality-sharing branch, respectively. Zhang et al. [21] achieve probabilistic cross-modal fusion through a generative architecture. Some methods also focus on addressing the challenge of depth ambiguity [24]–[27], [29], [41]. CFPF [24] designs a specific network to improve depth information, which is then fused with RGB features to enhance the contrast between foreground and background. Fan et al. [26] publish a large-scale dataset of human activity scenarios and design a three-stream module to filter unreliable depth maps. DCF [29] mitigates noise in low-quality depth maps through a calibration strategy. DMRA [41] utilizes RGB complementary cues to improve depth information. Recently, transformer-based methods [16], [30], [42]–[44] have demonstrated the superior performance due to their global modeling capability. VST [30] introduces the transformer into the salient object detection field for the first time, which models the global dependency of objects. The recent transformer-based method CAVER [43] designs a novel attention mechanism to integrate multi-scale and multi-modal features and propagate the global context.

The above methods exploit the complementary information between the modalities through different fusion strategies and obtain performance gains. However, they can still fall into performance bottlenecks when facing some challenging scenarios, such as depth ambiguity or thermal crossover, low illumination, image clutter, etc. Although some methods [26], [29], [43] can solve specific challenges, they also fail to address multiple challenges simultaneously. To deal with the major challenges in multi-modal SOD, we propose the adaptive fusion bank, which integrates multiple fusion schemes tailored for different challenges and adaptively selects appropriate fusion schemes according to the input data.

III. THE PROPOSED METHOD

In this section, we present an overview of our proposed learning adaptive fusion bank (LAFB) and elaborate on its key components, including the adaptive fusion bank and the indirect interactive guidance module. We also describe the loss function used in our method.

A. Overview

As shown in Fig. 2, our LAFB model is based on an encoder-decoder framework. First, the multi-modal images are separately fed into the encoder, which is built on the Res2Net-50 [45] network. The encoder extracts hierarchical multi-modal features, denoted as f_i^r and $f_i^{t/d}$, where r represents the RGB modality, t/d represents the thermal or depth modality, and $i \in \{1, 2, \dots, 5\}$ denotes different layers. To reduce computation, we discard the lowest feature maps, i.e., f_1^r and $f_1^{t/d}$. Next, in the decoder stage, we use top-down inference to integrate the hierarchical features and predict saliency maps.

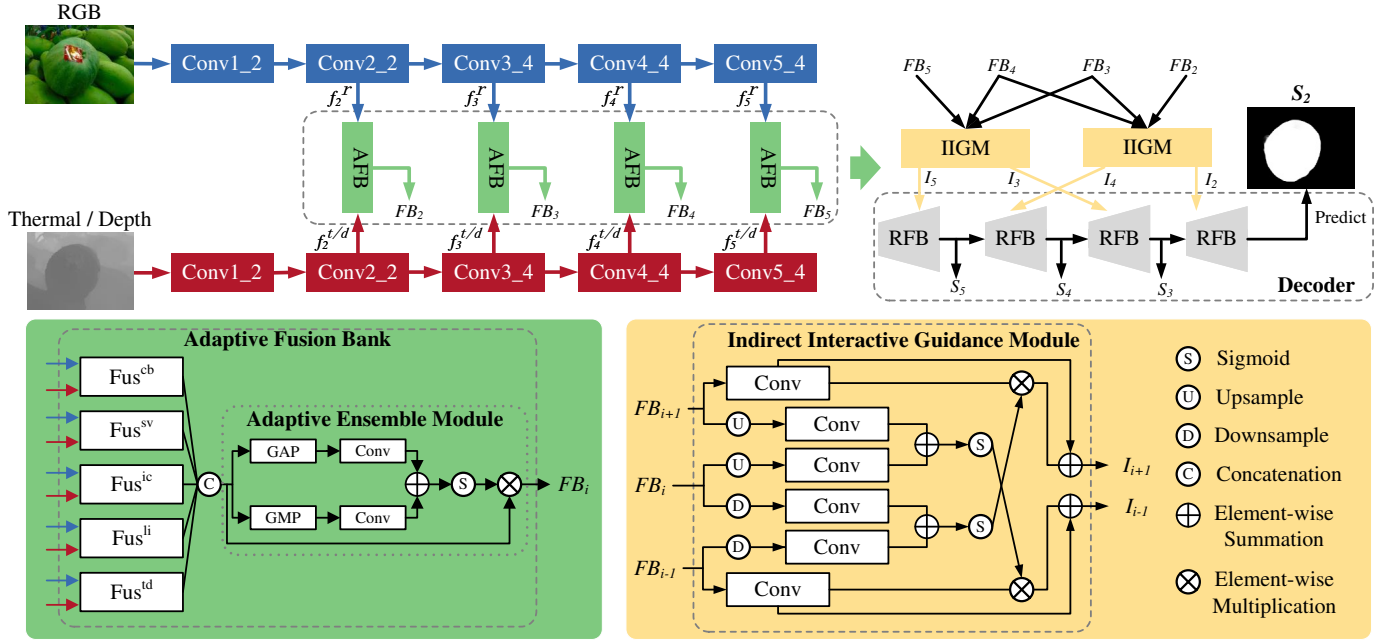


Fig. 2. Overview of our proposed learning adaptive fusion bank (LAFB). We first send the extracted multi-modal features (i.e., f_i^r and $f_i^{t/d}$) into the adaptive fusion bank (AFB), which contains five specific fusion schemes (i.e., Fus^{cb} , Fus^{sv} , Fus^{ic} , Fus^{li} and Fus^{td}) to generate multi-level features (i.e., FB_i) for corresponding challenges. Then, the multi-level features are fed into the indirect interactive guidance module (IIGM) to integrate high-level and low-level features smoothly. After that, the generated features (i.e., I_i) are fed into the RFB module to increase the receptive field of features. Finally, multi-level saliency maps (i.e., S_i) are inferred in a top-down manner in the decoder, and S_2 is taken as the final saliency map.

Adaptive fusion bank (AFB) and indirect interactive guidance module (IIGM) are the two key components of our LAFB. AFB is designed to leverage the complementary benefits of multiple fusion schemes for addressing different challenges. As shown in Fig. 2, each bank consists of five different fusion schemes and an adaptive ensemble module. The extracted features are sent into AFB and decoupled by different fusion schemes for different challenges. Subsequently, the adaptive ensemble module aggregates the decoupled features to address current challenges, generating the multi-level features FB_i . Then, the IIGM takes three adjacent features (i.e., FB_{i-1} , FB_i and FB_{i+1} , $i \in \{3, 4\}$) as inputs to effectively integrate high-level semantic information and low-level detailed features. The integrated features I_i are then sent into the decoder to generate the final saliency map S_2 in a top-down manner.

B. Adaptive Fusion Bank

In the multi-modal salient object detection (MSOD) task, the design of fusion schemes can affect the quality of the fused features and the model performance. Existing MSOD methods [13], [14], [19]–[21] focus on designing complex fusion strategies to exploit multi-modal complementarity, which achieve performance improvements. However, they also fall into performance bottlenecks when faced with challenging scenarios, such as those with depth ambiguity, low illumination, image clutter, etc. To solve this problem, some recent methods [1], [22], [22], [23] design fusion strategies to cope with certain challenges. Nonetheless, these fusion strategies are tailored for specific challenges, and they hardly generate rich salient cues in other common challenging scenes.

To address multiple major challenges simultaneously, we propose to design a fusion bank comprising different fusion schemes that can adaptively select appropriate schemes for different challenges in the input data. There are two important issues that need to be addressed. First, how to design these fusion schemes so that can effectively handle different challenges. Second, how to select appropriate fusion schemes for the different challenges of multi-modal inputs. Therefore, we design the adaptive fusion bank to solve these two issues, as depicted in Fig. 2.

Fusion schemes: Building upon the work [14], which has described the challenges of RGBT SOD in detail, we identify the main challenges in MSOD as follows: modality-shared challenges, including center bias (CB), scale variation (SV), and image clutter (IC), and modality-specific challenges, including low illumination (LI), thermal crossover or depth ambiguity (TD). Considering the different characteristics of these main challenges, we design the corresponding five basic fusion schemes to solve the first problem mentioned above, as shown in Fig. 3. The fusion schemes are designed to be simple in structure. There are several reasons for this. First, considering the overall computation complexity of the adaptive fusion bank that is embedded into each encoder layer, we design each fusion scheme with simple but effective structure. Second, the limited amount of multi-modal data makes it difficult to learn a large number of parameters for each challenge using complex fusion schemes, while a few parameters in simple fusion schemes are easier to be learned. Third, these fusion schemes share the same backbone, which extracts rich and common features. Hence, each fusion scheme only requires a simple tailored design to decouple effective

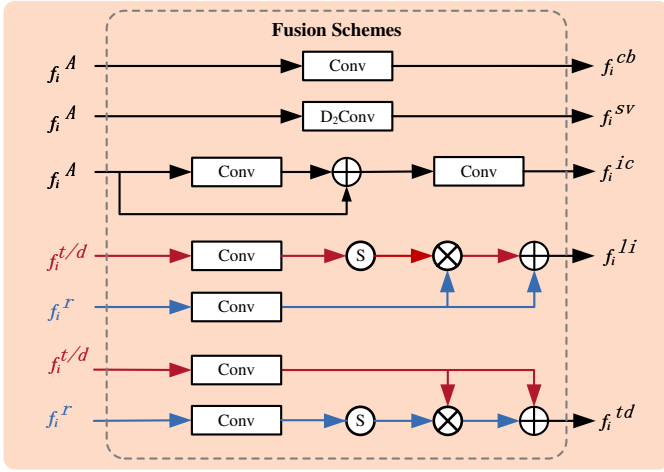


Fig. 3. Architectures of the fusion schemes in the adaptive fusion bank. f_i^A represents the concatenation of multi-modal features (i.e., $f_i^{t/d}$ and f_i^r) extracted by the backbone. f_i^{cb} , f_i^{sv} , f_i^{ic} , f_i^{li} and f_i^{td} are generated by the corresponding fusion schemes for different challenges.

features for the specific challenge.

Center bias is a relatively simple challenge, objects with center-bias are usually close to the image boundary and mainly need to be located. Although complex and deep fusion structures have a strong positioning ability, they also have high computational complexity. Considering the overall computational complexity of AFB, we adopt a simple and effective design for Fus^{cb} . Since the backbone has already extracted rich features, the center bias fusion scheme only needs to decouple the location information of the object from it. Therefore, we use a convolutional block with a 3×3 kernel size to extract the extracted features at each location by sliding, so that the features of objects can be captured as much as possible. In addition, center bias is a common challenge that usually accompanied with other challenges [14]. By combining with other fusion schemes, Fus^{cb} is able to more accurately locate salient objects with the help of global features generated by other complex fusion schemes. This fusion scheme, denoted as Fus^{cb} , is designed to address center bias and can be formulated as follows:

$$f_i^{cb} = Conv(f_i^A), \quad (1)$$

where $f_i^A = [f_i^r, f_i^{t/d}]$ represents the concatenation of multi-modal features extracted by the backbone, and $Conv(\cdot)$ means a convolution layer. f_i^{cb} is the output of the i_{th} multi-modal feature f_i^A through the fusion scheme Fus^{cb} .

In the case of the scale variation challenge, the size of salient objects are variable and the number of salient objects can be single or multiple. Therefore, a wide receptive field is necessary to fully capture the scale-varying objects. The original convolutional block focuses on local areas and is difficult to cover the large or multiple objects effectively. To address this, we utilize a dilated convolution, which is specialized in increasing the receptive field and beneficial for capturing the large or multiple objects. Specifically, we use a convolutional layer with a 3×3 kernel size and a dilation

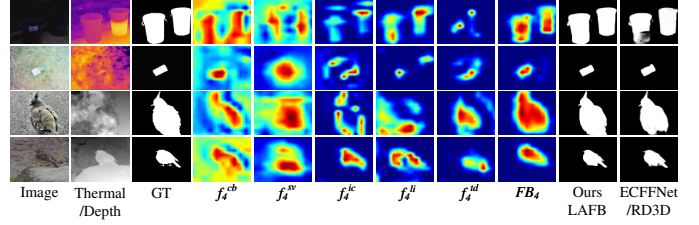


Fig. 4. Visualization of feature maps generated by different fusion schemes and adaptive ensemble module in the 5^{th} adaptive fusion bank. From the 1^{st} row to the 4^{th} row, the challenge is low light, thermal crossover, depth ambiguity and image clutter, respectively. The results of the saliency maps indicate that our method is able to deal with multiple challenges simultaneously, while the comparison methods (i.e., ECFFNet [23] and EBFSP [46]) fails on some challenges, such as the first and the third rows.

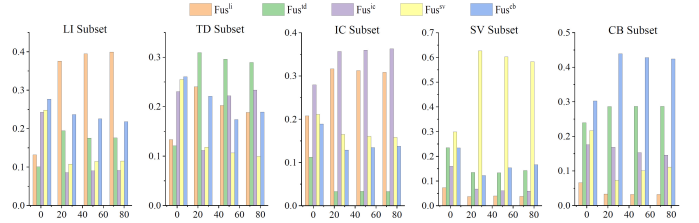


Fig. 5. Weights assigned to different fusion schemes when training on different challenge data, which are all obtained based on the challenge annotation of the training set of VT5000. The x-axis and y-axis represent the training epochs and weights, respectively. The values of columns in different colors indicate the weight assigned to different fusion schemes during training.

rate of 2 for the Fus^{sv} fusion scheme. This process can be formulated as follows:

$$f_i^{sv} = D_2Conv(f_i^A), \quad (2)$$

where f_i^{sv} denotes the features generated by the fusion scheme Fus^{sv} , $D_2Conv(\cdot)$ is the dilated convolution with dilation rate 2.

Image clutter is a relatively difficult challenge, caused by low contrast between foreground and background, complex background, etc. As shown in the fifth row of Fig. 1, under the image clutter challenge, too much noise exists in the background, which prevents the network from detecting salient objects accurately. To this end, we first localize the salient regions in an image. Specifically, we use two consecutive convolutional blocks to obtain features with a larger field of view containing global and semantic information that can help identify regions of the image. Second, we finely separate the salient regions from the background. Specifically, we introduce the initial input features through a residual connection. Due to the relatively small receptive field, the initial features have rich spatial details, such as textures, boundaries, etc., which can make salient and non-salient areas more distinguishable. In this way, salient objects in the image clutter challenge scene can be accurately recognized and separated out. We obtain the output feature f_i^{ic} of this fusion scheme Fus^{ic} as follows:

$$f_i^{ic} = Conv(Conv(f_i^A) + f_i^A). \quad (3)$$

Low illumination is a challenge specific to the RGB modality. In this case, it is difficult to capture a clear object

appearance from RGB images, while thermal or depth images tend to contain more sufficient object information. Therefore, it is challenging for RGB modality to cope with this type of challenge due to feature degradation. To address this challenge, we introduce the features of the thermal or the depth modality to compensate for the lack of information. In detail, we first smooth the features of the thermal or the depth modality with a 3×3 convolutional block to reduce noise in them. Since thermal or depth modality captures objects more explicitly than RGB modality in the low illumination scenario, we use a Sigmoid activation function σ to obtain the weight distribution W_{td} of the thermal or the depth features, highlighting the object's location. Then, we perform the multiplication of the weight W_{td} and RGB features to guide RGB features to focus on the object region. Considering the information loss caused by multiplication, we maintain RGB information by summing the original RGB features with the guided RGB features. The process of the fusion scheme Fus^{li} can be described as follows:

$$W_{td} = \sigma(\text{Conv}(f_i^{t/d})), \quad (4)$$

$$f_i^{li} = W_{td} \odot f_i^r + f_i^r, \quad (5)$$

where \odot represents an element-wise multiplication.

Thermal crossover or depth ambiguity is another modality-specific challenge. In this case, the object features of thermal or depth images are degenerated, while RGB images tend to have more complete object information. To deal with this challenge, we use the features of the RGB modality as an information supplement. Hence, we design a fusion scheme Fus^{td} similar to the fusion scheme used for the low illumination challenge. This process can be formulated as:

$$W_r = \sigma(\text{Conv}(f_i^r)), \quad (6)$$

$$f_i^{td} = W_r \odot f_i^{t/d} + f_i^{t/d}. \quad (7)$$

Note that although the modality-specific fusion schemes are similar to the spatial attention mechanism [34] and the cross-modal fusion of the method [24], their impact is completely different. The spatial attention mechanism and the cross-modal fusion of the method [24] both refine feature representations in general, without a specific objective. Instead, our modality-specific fusion schemes are tailored for low illumination, thermal crossover, or depth ambiguity challenges. By being combined with other fusion schemes and adaptively assigned training weights based on the challenges in the input data through AEM, the modality-specific fusion schemes can be effectively trained and further decouple the extracted features to deal with the modality-specific challenges.

Adaptive ensemble module: Although each fusion scheme can address a specific challenge, the input data is dominated by different challenges, which means that each input data may require a different combination of fusion schemes. Therefore, it is necessary to select appropriate fusion schemes according to the challenges present in the input data. To address this issue, we propose an adaptive ensemble module (AEM) to select the fusion schemes that effectively address challenges in the input

data. AEM integrates these fusion schemes by learning the weights of features generated by them. As illustrated in Fig. 2, AEM is designed inspired by channel attention [34], which is usually used to refine independent features. Unlike channel attention, our AEM is responsible for adaptively integrating features that can effectively deal with different challenges. In this way, the fusion schemes designed for current challenges can be selected effectively.

Specifically, we first concatenate all the fused features of the fusion schemes in the channel dimension, which is denoted as f_i^C . Then, a global average pooling layer (*GAP*) and a global max pooling layer (*GMP*) followed by one 1×1 convolutional layer are separately adopted, which compress the spatial dimension of the concatenated feature from two aspects. After that, we perform pixel-wise addition operation on the two compressed features and then utilize a Sigmoid function to learn the channel weight vector $V \in \mathbb{R}^{c \times 1 \times 1}$, in which the c represents the number of channels of the feature. The formulation of this procedure can be expressed as:

$$f_i^C = [f_i^{cb}, f_i^{sv}, f_i^{ic}, f_i^{li}, f_i^{td}], \quad (8)$$

$$V = \sigma(\text{Conv}(\text{GAP}(f_i^C)) + \text{Conv}(\text{GMP}(f_i^C))), \quad (9)$$

where $[, \dots,]$ represents the channel-wise concatenation. Then the features of each fusion scheme is weighted by the vector V , as:

$$FB_i = V \odot f_i^C, \quad (10)$$

where FB_i is the output feature of the i_{th} layer fusion bank. At this point, the second problem mentioned above has also been solved.

In Fig. 4, the visualization results show that the extracted multi-modal features decoupled by different fusion schemes are specialized in handling different challenges. For each multi-modal input, the fusion schemes for the challenges in the input data can decouple the extracted features with more saliency cues. Besides, the feature maps generated by AEM always have the highest response to the objects. This demonstrates that the fusion schemes are effective in addressing different challenges and the AEM can make them complementary to achieve adaptive integration.

To further illustrate that the proposed fusion schemes in AFB can be trained specifically, we train the network separately with different challenge datasets annotated in the training set of VT5000 [14]. During training, we obtain the weight assigned to each fusion scheme, which is separated from the weight vector V . The weight changes of different fusion schemes on different challenge datasets are shown in Fig. 5. Note that each subset of challenge data is derived from the training set of the VT5000 [14] and is obtained according to its challenge annotation. More details regarding the challenge annotation can be referred to [14]. It can be seen that AFB assigns larger weights to the fusion schemes tailored to the current input challenges, since they can generate features with more salient cues. In this way, for different input data, the corresponding fusion schemes can be trained with bigger gradients. Furthermore, with the iteration of training,

each fusion scheme can learn corresponding parameters to deal with corresponding challenges more effectively, and AEM will also assign a greater weight to the fusion scheme that meets the current challenges, as shown in Fig. 5. Therefore, each fusion scheme can be fully trained by the corresponding challenge data to deal with their respective challenges.

C. Indirect Interactive Guidance Module

After the adaptive fusion bank integrates the multi-modal features, hierarchical features FB_i are obtained. Low-level detailed features contain rich detailed information, such as texture, color, boundary, etc., which can make the foreground and background more distinguishable. High-level features provide sufficient semantic information that facilitates category recognition and the localization of salient regions from background. By integrating multi-level features, richer features can be obtained for accurate segmentation in complex scenes, such as the hollow objects. Existing methods [1], [2], [29]–[31] often use top-down fusion to integrate features layer by layer, which limits feature variety and prevents full fusion of high-level and low-level features. Some other methods [28], [33] directly integrate multi-level features to generate richer features for each layer, but they fail to fully exploit the unique characteristics of high-level and low-level features. Furthermore, direct integration of multi-level features may compromise the original information contained in these features.

To address the above problem, we propose an indirect interactive guidance module that exploits the unique characteristics of high-level and low-level features to achieve mutual guidance of multi-level features. Besides, by introducing an intermediate feature, high-level and low-level features can be integrated indirectly, so as to preserve the origin information in them as much as possible. As shown in Fig. 2, we use three successive multi-modal features (FB_{i-1} , FB_i and FB_{i+1} , $i \in \{3, 4\}$) as inputs, which contain both high-level semantic features (FB_4 and FB_5) and low-level detail features (FB_2 and FB_3). Then, we take the intermediate FB_i as a springboard to fuse the high-level feature FB_{i+1} with the low-level feature FB_{i-1} interactively. With this springboard, high-level features and low-level features can be smoothly associated without intermediate information gaps. In detail, on the one hand, we first up-sample FB_i and FB_{i+1} to the size of FB_{i-1} , and send them into the convolutional layer with a 3×3 kernel size separately. Then we fuse them by a pixel-wise addition and apply a Sigmoid function to learn the high-level weight W_{high} , which is used to guide the low-level feature FB_{i-1} . The whole process can be formulated as follows:

$$W_{high} = \sigma(\text{Conv}(Us(FB_i)) + \text{Conv}(Us(FB_{i+1}))). \quad (11)$$

$Us(\cdot)$ indicates the upsample operation with bilinear interpolation. On the other hand, we down-sample FB_i and FB_{i-1} to the size of FB_{i+1} , then do same operations as above to generate the weight to guide FB_{i+1} , as follows:

$$W_{low} = \sigma(\text{Conv}(Ds(FB_{i-1})) + \text{Conv}(Ds(FB_i))), \quad (12)$$

where W_{low} is the low-level weight and $Ds(\cdot)$ indicates the down-sample operation with bilinear interpolation. Then, we

perform element-wise multiplication of W_{low} with FB_{i+1} and W_{high} with FB_{i-1} respectively to form the guidance. To retain the details, we add the original features FB_{i+1} and FB_{i-1} , separately. The whole process can be formulated as follows:

$$\begin{aligned} I_{i+1} &= FB_{i+1} + FB_{i+1} \odot W_{low}, \\ I_{i-1} &= FB_{i-1} + FB_{i-1} \odot W_{high}, \end{aligned} \quad (13)$$

where I_{i+1} and I_{i-1} are the output features of the indirect interactive guidance module.

In the decoder, the integrated features I_i are fused in a top-down manner, as in U-Net [47]. Besides, following [2], we embed the receptive field block (RFB) [48] into the process to increase the receptive field of features. Then the final saliency map S_2 is predicted from the lowest fused feature by a 1×1 convolutional layer and an upsample operation.

D. Loss Function

Similar to previous works [2], [36], we employ the binary cross-entropy loss to calculate the distance between the final predicted saliency map and the ground truth. To allow our model to learn discriminative information, we also use the binary cross-entropy loss on the remaining features of the decoder, i.e.,

$$\ell_i = \ell_{bce}(S_i, G), i = 2, 3, 4, 5. \quad (14)$$

Where ℓ_{bce} represents the binary cross-entropy loss, G is the ground truth, S_i consists the final saliency map S_2 and the intermediate saliency maps $\{S_i\}_{i=3}^5$ produced from the remaining features of the decoder.

Following [36] and [49], we also use the smoothness loss [50] ℓ_s and dice loss [51] ℓ_d for the final saliency map S_2 to keep the boundary clear and the region consistent. Therefore, the total loss function can be expressed as:

$$\ell_{total} = \sum_{i=2}^5 \lambda_i \ell_i + \ell_s + \ell_d, \quad (15)$$

where λ_i denote the weights of different losses, and we set the values of λ_2 , λ_3 , λ_4 and λ_5 to 1.0, 0.8, 0.6, 0.5 respectively. The ablation study and specific analysis are presented in Sec. IV-C.

IV. EXPERIMENT

A. Experimental Setup

1) *Datasets*: We conduct RGBD experiments on seven challenging RGBD datasets, including DUT-RGBD [25] (i.e., DUT), NJUD [56], NLPR [55], SIP [26], SSD [52], STERE [53], and ReDWeb-S [54]. Following [71], we take a collection of 700 samples from NLPR, 1485 samples from NJUD and 800 samples from DUT-RGBD as our RGBD training set and all the remaining image pairs as testing set.

The following RGBT experiments are conducted on three existing RGBT datasets, including VT821 [11], VT1000 [12] and VT5000 [14]. For a fair comparison, we train our network with the training set in VT5000, and take all image pairs in

TABLE I
QUANTITATIVE COMPARISON OF E-MEASURE (E_{ξ}), WEIGHED F-MEASURE (F_{β}^{ω}), F-MEASURE (F_{β}), MEAN ABSOLUTE ERROR (MAE) AND FRAME-PER-SECOND (FPS) WITH 17 DIFFERENT RGBD METHODS ON SEVEN TESTING DATASETS, INCLUDING SIP [26], DUT-RGBD [25] (I.E., DUT), SSD [52], STERE [53], REDWEB-S [54], NLPR [55], AND NJUD [56]. THE BEST, SECOND BEST AND THIRD BEST RESULTS ARE MARKED WITH RED AND GREEN, RESPECTIVELY. ‘-’ INDICATES THE CODE OR RESULT IS NOT AVAILABLE.

Methods	Backbone	SIP [26]				DUT [25]				SSD [52]				STERE [53]				RedWeb-S [54]				NLPR [55]				NJUD [56]				FPS \uparrow	Param \downarrow	GFLOPs \downarrow
		E_{ξ} \uparrow	F_{β}^{ω} \uparrow	F_{β} \uparrow	MAE \downarrow	E_{ξ} \uparrow	F_{β}^{ω} \uparrow	F_{β} \uparrow	MAE \downarrow	E_{ξ} \uparrow	F_{β}^{ω} \uparrow	F_{β} \uparrow	MAE \downarrow	E_{ξ} \uparrow	F_{β}^{ω} \uparrow	F_{β} \uparrow	MAE \downarrow	E_{ξ} \uparrow	F_{β}^{ω} \uparrow	F_{β} \uparrow	MAE \downarrow	E_{ξ} \uparrow	F_{β}^{ω} \uparrow	F_{β} \uparrow	MAE \downarrow	E_{ξ} \uparrow	F_{β}^{ω} \uparrow	F_{β} \uparrow	MAE \downarrow			
HDFNet ₂₀ [57]	VGG19	0.920	0.848	0.862	0.048	0.937	0.873	0.887	0.040	0.902	0.823	0.831	0.047	0.924	0.863	0.860	0.041	0.760	0.623	0.704	0.133	0.949	0.873	0.874	0.028	0.911	0.879	0.856	0.039	77	164.19	111.02
CoNet ₂₀ [58]	ResNet101	0.909	0.814	0.842	0.063	0.948	0.896	0.909	0.033	0.896	0.792	0.806	0.059	0.928	0.874	0.885	0.037	0.762	0.618	0.688	0.147	0.934	0.850	0.848	0.031	0.912	0.856	0.873	0.046	154	162.13	13.05
CCAFNet ₂₁ [31]	ResNet50	0.915	0.839	0.864	0.054	0.940	0.884	0.903	0.037	0.915	0.839	0.864	0.054	0.921	0.853	0.869	0.044	0.687	0.515	0.614	0.173	0.951	0.883	0.880	0.026	0.920	0.883	0.896	0.037	88	159.45	189.47
CDNet ₂₁ [59]	VGG16	0.913	0.839	0.870	0.056	0.936	0.878	0.901	0.039	0.849	0.706	0.742	0.073	0.929	0.871	0.884	0.039	0.730	0.588	0.678	0.146	0.951	0.886	0.879	0.025	0.903	0.828	0.856	0.054	86	123.65	72.07
HAI-Net ₂₁ [27]	VGG16	0.924	0.860	0.883	0.049	0.937	0.887	0.905	0.038	0.843	0.682	0.735	0.101	0.930	0.877	0.888	0.038	0.766	0.654	0.713	0.132	0.951	0.884	0.884	0.025	0.917	0.882	0.895	0.039	11	228.20	181.62
DFM ₂₁ [60]	MobileNetV2	0.919	0.844	0.871	0.051	0.898	0.795	0.830	0.062	0.871	0.733	0.755	0.076	0.912	0.850	0.858	0.045	0.753	0.610	0.690	0.136	0.945	0.876	0.868	0.026	0.913	0.868	0.885	0.042	252	8.45	5.43
SPNet ₂₁ [2]	Res2Net50	0.930	0.873	0.891	0.043	0.876	0.747	0.843	0.085	0.910	0.831	0.852	0.044	0.930	0.879	0.886	0.037	0.759	0.637	0.712	0.129	0.957	0.899	0.898	0.021	0.931	0.909	0.915	0.029	50	573.39	68.10
RD3D ₂₁ [61]	13DResNet50	0.919	0.852	0.873	0.049	0.949	0.913	0.925	0.031	0.905	0.794	0.812	0.052	0.926	0.877	0.885	0.038	0.701	0.487	0.595	0.177	0.957	0.894	0.890	0.022	0.918	0.890	0.900	0.037	94	110.30	43.51
DSA2F ₂₁ [28]	VGG19	0.908	0.838	0.867	0.057	0.950	0.914	0.926	0.030	0.904	0.836	0.852	0.047	0.928	0.877	0.895	0.038	-	-	-	-	0.950	0.889	0.897	0.024	0.923	0.889	0.901	0.039	-	-	-
DCF ₂₁ [29]	ResNet50	0.920	0.850	0.877	0.051	0.952	0.913	0.925	0.030	0.898	0.800	0.829	0.053	0.931	0.880	0.890	0.037	0.755	0.632	0.710	0.135	0.956	0.892	0.893	0.023	0.922	0.884	0.897	0.038	57	111.51	59.38
MobileSal ₂₁ [49]	MobileNetV2	0.914	0.837	0.860	0.054	0.936	0.869	0.912	0.044	0.898	0.804	0.815	0.052	0.916	0.865	0.848	0.041	0.671	0.455	0.608	0.186	0.950	0.878	0.872	0.025	0.914	0.874	0.894	0.040	268	24.97	1.96
SSL ₂₂ [62]	VGG16	0.921	0.851	0.875	0.049	0.927	0.859	0.888	0.046	0.833	0.638	0.696	0.100	0.923	0.864	0.875	0.042	-	-	-	-	0.954	0.885	0.884	0.027	0.881	0.786	0.821	0.065	52	282.95	272.20
DIGRNet ₂₂ [63]	ResNet50	0.918	0.849	0.878	0.053	0.948	0.902	0.919	0.033	0.889	0.804	0.823	0.053	0.927	0.877	0.888	0.038	-	-	-	-	0.955	0.895	0.888	0.023	0.928	0.909	0.916	0.028	33	635.79	68.16
CIRNet ₂₂ [64]	ResNet50	0.917	0.848	0.874	0.053	0.951	0.908	0.926	0.031	0.898	0.791	0.821	0.054	0.921	0.836	0.875	0.049	0.725	0.519	0.630	0.171	0.955	0.889	0.883	0.023	0.922	0.881	0.896	0.040	93	393.50	42.60
MoADNet ₂₂ [65]	MobileNetV3	0.908	0.828	0.850	0.058	0.949	0.911	0.923	0.031	0.894	0.801	0.824	0.057	0.914	0.861	0.868	0.042	-	-	-	-	0.945	0.875	0.874	0.027	0.909	0.881	0.892	0.041	167	19.19	1.32
LSNet ₂₂ [66]	MobileNetV2	0.927	0.856	0.882	0.049	0.891	0.775	0.831	0.074	0.902	0.796	0.820	0.055	0.913	0.827	0.854	0.054	0.691	0.458	0.566	0.193	0.955	0.881	0.882	0.024	0.922	0.885	0.899	0.038	316	17.41	3.04
CAVER ₂₃ [43]	ResNet50	0.927	0.874	0.884	0.043	0.955	0.920	0.919	0.029	0.915	0.826	0.828	0.044	0.931	0.887	0.871	0.034	0.760	0.663	0.724	0.121	0.959	0.899	0.894	0.022	0.922	0.903	0.874	0.032	67	212.83	218.64
Ours	VGG16	0.912	0.836	0.863	0.055	0.939	0.890	0.906	0.039	0.901	0.800	0.828	0.047	0.921	0.861	0.876	0.042	0.748	0.612	0.688	0.143	0.954	0.891	0.896	0.024	0.918	0.894	0.904	0.036	40	398.05	552.10
Ours	ResNet50	0.919	0.850	0.878	0.051	0.951	0.911	0.923	0.031	0.919	0.842	0.865	0.041	0.927	0.870	0.886	0.040	0.763	0.653	0.719	0.133	0.955	0.894	0.896	0.024	0.918	0.897	0.906	0.033	50	451.80	137.68
Ours	Res2Net50	0.937	0.883	0.902	0.041	0.957	0.919	0.930	0.027	0.922	0.840	0.860	0.041	0.930	0.882	0.896	0.037	0.757	0.664	0.727	0.128	0.958	0.902	0.905	0.021	0.924	0.910	0.919	0.028	45	453.03	139.73

TABLE II
QUANTITATIVE COMPARISON OF E-MEASURE (E_{ξ}), WEIGHED F-MEASURE (F_{β}^{ω}), F-MEASURE (F_{β}), MEAN ABSOLUTE ERROR (MAE) AND FRAME-PER-SECOND (FPS) WITH 14 DIFFERENT RGBT METHODS ON THREE TESTING DATASETS, INCLUDING VT5000 [14], VT1000 [12] AND VT821 [11]. THE BEST, SECOND BEST AND THIRD BEST RESULTS ARE MARKED WITH RED AND GREEN, RESPECTIVELY

Methods	Backbone	VT5000 [14]				VT1000 [12]				VT821 [11]				FPS \uparrow	Param \downarrow	GFLOPs \downarrow
		E_{ξ} \uparrow	F_{β}^{ω} \uparrow	F_{β} \uparrow	MAE \downarrow	E_{ξ} \uparrow	F_{β}^{ω} \uparrow	F_{β} \uparrow	MAE \downarrow	E_{ξ} \uparrow	F_{β}^{ω} \uparrow	F_{β} \uparrow	MAE \downarrow			
MTMR ₁₈ [10]	-	0.795	0.397	0.595	0.114	0.836	0.485	0.715	0.119	0.815	0.462	0.662	0.108	-	-	-
M3S-NIR ₁₉ [67]	-	0.780	0.327	0.575	0.168	0.827	0.463	0.717	0.145	0.859	0.407	0.734	0.407	-	-	-
SGDL ₁₉ [12]	-	0.824	0.559	0.672	0.089	0.856	0.652	0.764	0.090	0.847	0.583	0.730	0.085	-	-	-
ADF ₂₀ [14]	VGG16	0.891	0.722	0.778	0.048	0.921	0.804	0.847	0.034	0.842	0.627	0.077	0.716	27	254.67	191.45
MIDD ₂₁ [36]	VGG16	0.897	0.763	0.801	0.043	0.933	0.856	0.882	0.027	0.895	0.760	0.804	0.045	33	200	216.72
CSRNet ₂₁ [19]	ESPNetV2	0.905	0.796	0.811	0.042	0.925	0.878	0.877	0.024	0.909	0.821	0.831	0.038	-	-	-
CGFNet ₂₁ [1]	VGG16	0.922	0.831	0.851	0.035	0.944	0.900	0.906	0.023	0.912	0.829	0.845	0.038	18	266.73	347.78
MMNet ₂₁ [68]	Res2Net50	0.887	0.770	0.780	0.043	0.923	0.863	0.861	0.027	0.892	0.783	0.794	0.040	-	-	-
ECFFNet ₂₁ [23]	ResNet34	0.906	0.802	0.807	0.038	0.93	0.885	0.876	0.021	0.902	0.801	0.810	0.034	-	-	-
MIA-DPP ₂₂ [69]	ResNet50	0.893	0.780	0.793	0.040	0.926	0.864	0.868	0.025	0.850	0.720	0.741	0.070	-	-	-
OSRNet ₂₂ [70]	ResNet50	0.908	0.807	0.823	0.040	0.935	0.891	0.892	0.022	0.896	0.801	0.814	0.043	142	59.67	51.27
DCNet ₂₂ [37]	VGG16	0.920	0.819	0.847	0.035	0.948	0.902	0.911	0.021	0.912	0.823	0.841	0.037	43	91.57	207.21
LSNet ₂₃ [66]	MobileNetV2	0.915	0.806	0.825	0.037	0.935	0.887	0.885	0.023	0.911	0.809	0.825	0.033	314	17.41	3.04
CAVER ₂₃ [43]	ResNet50	0.924	0.835	0.841	0.032	0.945	0.909	0.903	0.017	0.919	0.835	0.839	0.033	67	451.8	137.68
Ours	VGG16	0.917	0.825	0.838	0.035	0.939	0.899	0.897	0.021	0.904	0.810	0.824	0.038	37	398.05	552.1
Ours	ResNet50	0.925	0.829	0.847	0.032	0.944	0.900	0.902	0.019	0.910	0.802	0.831	0.034	49	451.8	137.68
Ours	Res2Net50	0.931	0.841	0.857	0.030	0.945	0.905	0.905	0.018	0.915	0.817	0.843	0.034	43	453.03	

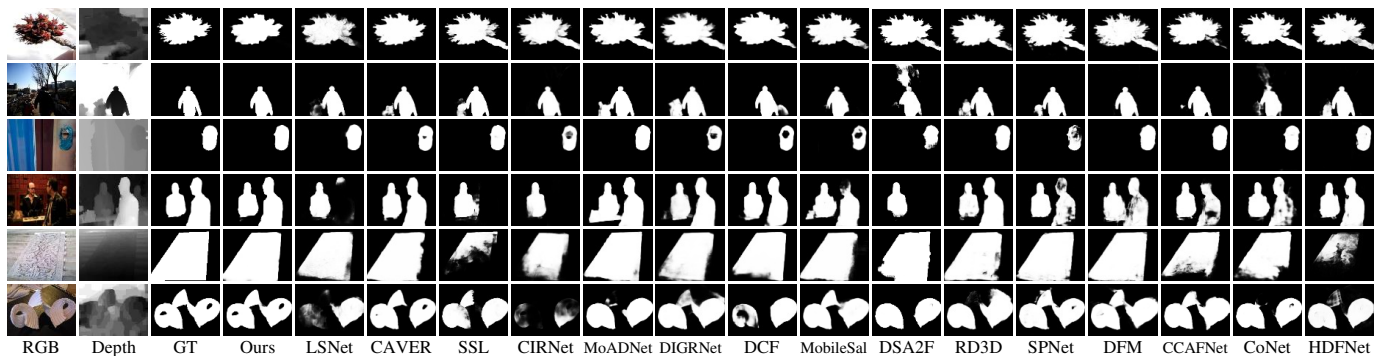


Fig. 6. Qualitative visual comparisons of the proposed method with other RGBD methods in diverse challenges. From the 1st row to the 5th row, they are mainly challenged by depth ambiguity, low illumination, center bias, number variation and image clutter respectively. The 6th shows the case of hollow object.

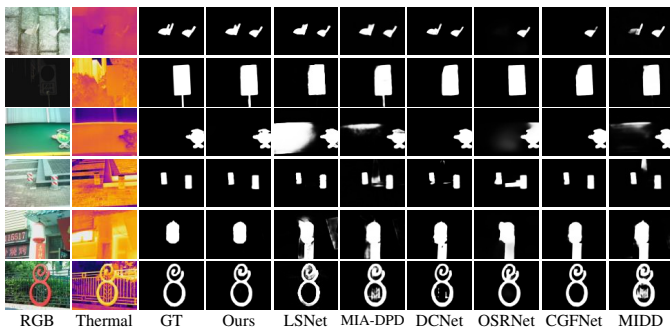


Fig. 7. Qualitative visual comparisons of the proposed method with other RGBT methods in diverse challenges. From the 1st row to the 5th row, they are mainly challenged by thermal crossover, low illumination, center bias, number variation and image clutter respectively. The 6th shows the case of hollow object.

TABLE III
PERFORMANCE COMPARISON RESULTS OF E-MEASURE (E_ξ),
F-MEASURE (F_β), AND MEAN ABSOLUTE ERROR (MAE) WITH 4
TRANSFORMER BACKBONE BASED METHODS ON VT5000 [14] TEST SET
FOR RGBT MODELS AND NJUD [56] TEST SET FOR RGBD MODELS.
THE BEST RESULTS ARE MARKED WITH **BOLD**.

Methods	Backbone	VT5000 [14]			NJUD [56]			STERE [53]		
		$E_\xi \uparrow$	$F_\beta \uparrow$	$MAE \downarrow$	$E_\xi \uparrow$	$F_\beta \uparrow$	$MAE \downarrow$	$E_\xi \uparrow$	$F_\beta \uparrow$	$MAE \downarrow$
VST ₂₁ [30]	T2T-ViT	-	-	-	0.913	0.856	0.035	0.916	0.844	0.038
SwinNet ₂₂ [44]	Swin Transformer	0.942	0.865	0.026	0.933	0.921	0.027	0.929	0.892	0.033
HRTransNet ₂₃ [16]	HRFormer	0.945	0.871	0.025	0.929	0.919	0.029	0.929	0.902	0.030
CAVER ₂₃ [43]	ResNet50	0.924	0.841	0.032	0.922	0.874	0.032	0.931	0.871	0.034
Ours	Swin Transformer	0.944	0.875	0.024	0.936	0.928	0.025	0.932	0.900	0.030

Net [59], HAINet [27], DFM [60], SPNet [2], RD3D [61], DSA2F [28], DCF [29], MobileSal [49], SSL [62], DIGRNet [63], CIRNet [64], MoADNet [65], LSNet [66], and CAVER [43]. For our RGBT model, we make a comparison with 14 RGBT SOD methods, including MTMR [10], M3S-NIR [67], SGDL [12], ADF [14], MIDD [36], CSRNet [19], CGFNet [1], MMNet [68], ECFFNet [23], MIA-DPD [69], OSRNet [70], DCNet [37], LSNet [66], and CAVER [43]. To make a fair comparison, we use the results published by the authors or by running their published code with default parameters.

2) *Quantitative Comparison*: Table I and Table II show

quantitative comparisons with RGBD SOD methods and RGBT SOD methods, respectively. These methods use different backbone networks. The backbone with deeper layers (i.e., ResNet50 [76], Res2Net50 [45]) provides networks [2], [43], [63], [64] with semantically richer features, which facilitates sufficient fusion and performance improvement but brings a larger number of parameters. In contrast, backbones with shallow layers (i.e., MobileNet [77], [78], VGG16 [79]) have low computational complexity and fast inference speed [37], [60], [65], [66], but at the expense of feature representation capability, resulting in inferior performance. Since the fusion schemes in our adaptive fusion bank (AFB) are basic and simple, designed to decouple the extracted features for different challenges, we use Res2Net-50 to extract rich features. For the RGBD comparison, our LAFB with Res2Net-50 outperforms other methods on most metrics across seven datasets. Even on the RedWeb-S [54] dataset with diverse scenes and object categories, LAFB still has superior performance, which demonstrates the effectiveness of our method. Compared with the advanced method SPNet [2], which also uses the Res2Net-50 backbone, our method achieves improvements of 0.8%, 1.1%, 1.2%, and 4.9% on the four metrics (E_ξ , F_β^ω , F_β and MAE) of the SIP dataset, respectively. CAVER [43] is a recent transformer-based method with strong global context modeling ability, and our method still has comparable performance against it. By replacing the backbone with ResNet50 or VGG16, our model achieves overall performance comparable to other state-of-the-art methods, such as LSNet [66], MoADNet [65] and SSL [62]. The results on GFLOPs show that the computational complexity of our method is acceptable. Similar to the advanced methods SPNet [2] and DIGRNet [63], there are many parameters in our method. This is mainly comes from the multiple fusion schemes in adaptive fusion bank, which also bring better performance. Table II shows the performance comparison of our method on three RGBT datasets. On the most challenging VT5000 dataset, our method achieves an average improvement of 2.5% on the four evaluation metrics, comparing with the advanced method CAVER [43]. On the VT821 and VT1000 datasets, our method is slightly inferior to CAVER, but still outperforms other CNN-based methods. This is mainly because on the relatively simple datasets, the global

TABLE IV
PERFORMANCE COMPARISON RESULTS OF MAX F-MEASURE ON 5 CHALLENGES. LI, TC, IC, SV AND CB REPRESENT THE CORRESPONDING CHALLENGE-ANNOTATED DATA IN THE TESTING SET OF VT5000 [14] FOR RGBT METHODS AND DUT-RGBD [25] FOR RGBD METHODS, RESPECTIVELY. THE BEST, SECOND BEST AND THIRD BEST RESULTS ARE MARKED WITH RED AND GREEN, RESPECTIVELY

Methods		LI	TC	IC	SV	CB
RGBT	MTMR [10]	0.691	0.597	0.585	0.661	0.599
	M3S-NIR [67]	0.700	0.608	0.567	0.633	0.588
	SGDL [12]	0.835	0.711	0.674	0.746	0.716
	ADF [14]	0.868	0.851	0.833	0.870	0.859
	MIDD [36]	0.894	0.866	0.841	0.875	0.871
	CSRNet [19]	0.873	0.864	0.811	0.867	0.847
	CGFNet [1]	0.891	0.896	0.864	0.886	0.883
	MMNet [68]	0.862	0.856	0.820	0.864	0.858
	ECFFNet [23]	0.870	0.872	0.835	0.880	0.870
	MIA-DPD [69]	0.892	0.889	0.852	0.888	0.882
	OSRNet [70]	0.873	0.842	0.833	0.880	0.866
	DCNet [37]	0.880	0.877	0.838	0.880	0.869
	LSNet [66]	0.898	0.865	0.848	0.881	0.869
	CAVER [43]	0.898	0.877	0.858	0.894	0.890
Ours LAFB	0.906	0.900	0.870	0.896	0.897	
RGBD	SPNet [2]	0.873	0.864	0.864	0.869	0.867
	RD3D [61]	0.939	0.932	0.932	0.944	0.942
	DSA2F [28]	0.935	0.929	0.946	0.936	0.937
	DCF [29]	0.938	0.935	0.934	0.937	0.933
	MobileSal [49]	0.922	0.916	0.940	0.927	0.930
	SSL [62]	0.913	0.880	0.907	0.907	0.915
	DIGRNet [63]	0.937	0.942	0.937	0.944	0.943
	CIRNet [64]	0.947	0.939	0.943	0.944	0.941
	MoADNet [65]	0.944	0.928	0.930	0.941	0.944
	LSNet [66]	0.883	0.870	0.846	0.866	0.862
	CAVER [43]	0.947	0.942	0.942	0.948	0.947
Ours LAFB	0.947	0.946	0.956	0.949	0.948	

modeling ability of transformer is not disturbed by various challenges and can perform better. Furthermore, we conduct a comparative analysis between our method and four recent transformer backbone based methods [16], [30], [43], [44]. For a fair comparison, we replace our CNN-based backbone with Swin Transformer [80], as employed in SwinNet [44]. The results in Table III show the overall superior performance of our method with the support of the transformer. Compared with the suboptimal method [16], our method achieves an average improvement of 6.7% on the *MAE* metric for the three datasets.

It is worth noting that most of these compared methods in Table I and Table II only perform one of the RGBD and RGBT tasks, but our method is applied to both tasks and achieves impressive performance. Our method demonstrates its strong generalization ability, as it is applied to both RGBD and RGBT tasks and achieves impressive performances, mainly due to the fusion schemes designed for the challenges in multi-modal images.

3) *Qualitative Comparison*: Fig. 6 and Fig. 7 illustrate the qualitative comparisons of our method against other top-

ranking methods in various challenging scenarios, including depth ambiguity or thermal crossover (the 1st row), low illumination (the 2nd row), center bias (the 3rd row), number variation (the 4th row) and image clutter (the 5th row). On the one hand, our method can segment salient regions more accurately in each case, whereas other methods only handle a few challenges well. For example, CIRNet [64] can handle the low illumination challenge (i.e., the 2nd row) well but fails on other challenges, and DCNet [37] can handle center bias and thermal crossover challenges (i.e., the 1st row and the 3rd row) well but also fails on other challenges. On the other hand, though some images contain multiple challenges, our method is able to exploit the complementarity of multiple fusion schemes to tackle them well, such as the 5th row in the RGBD comparison with the challenges of both image clutter and scale variation. The last row of both sets of comparisons is about the hollow object. The comparison results indicate that our method segment the foreground from background more precisely, which relies heavily on IIGM to balance semantic and detailed information.

4) *Challenge-based Comparison*: We further make a comparison with other methods on the five challenges labeled by VT5000 [14]. Following [22], [36], we compute the max F-measure score of each method on each challenge, and the results are presented in the upper part of Table IV. LI, TC, IC, SV and CB represent low illumination, thermal crossover, image clutter, scale variation and center bias challenges, respectively. On all challenges, our method outperforms the compared methods, which proves that our method can address these challenges simultaneously. The main reason is that our adaptive fusion bank can select corresponding fusion schemes to deal with challenges in different input data. Although CAVER [43], LSNet [66] and CGFNet [1] achieve sub-optimal performance on several challenges, they fail to perform well on all challenges at the same time. This demonstrates that the fusion strategies they designed focus on addressing specific challenges and have difficulty generating features for addressing some other important challenges. Note that the sub-optimal method CAVER [43] is a recent transformer-based method with a strong ability to model global contextual information, but it still performs poorly on some challenges that require both local and global information, such as the performance on image clutter (IC) challenge. Specifically, compared to it, our method achieves performance improvements of 0.9%, 2.6%, 1.4%, 0.2% and 0.8% on the five challenge (i.e., LI, TC, IC, SV, CB) data, respectively. Furthermore, on the center bias (CB) challenge, our method outperforms most methods (e.g., LSNet, DCNet, OSRNet) by a large margin, even though the fusion scheme used to solve the CB challenge only consists of one convolutional block. This validates that the fusion scheme we designed is simple but effective. In addition, following the rules in VT5000 [14], we annotate the challenge attributes of each image pair in the DUT-RGBD [25] dataset. Based on this, we also make a comparison with recent advanced RGBD SOD methods on the five challenges, and the results are shown in the lower part of Table IV. It can be found that our method also achieves optimality on all challenges, which demonstrates the effectiveness of our method to deal with the challenging

TABLE V

ABLATION STUDIES ON RGBD DATASETS, INCLUDING DUT-RGBD [25] TEST SET, NJUD [56] TEST SET AND STERE [53] DATASET. *w/o* MEANS TO DISCARD THE CORRESPONDING COMPONENT. THE BEST RESULTS ARE MARKED WITH **BOLD**. AFB: ADAPTIVE FUSION BANK, AEM: ADAPTIVE ENSEMBLE MODULE, AND IIGM: INDIRECT INTERACTIVE GUIDANCE MODULE

Models	DUT [25]				NJUD [56]				STERE [53]				FPS \uparrow	parameters(M) \downarrow	GFLOPs \downarrow
	$E_\xi \uparrow$	$F_\beta^\omega \uparrow$	$F_\beta \uparrow$	MAE \downarrow	$E_\xi \uparrow$	$F_\beta^\omega \uparrow$	$F_\beta \uparrow$	MAE \downarrow	$E_\xi \uparrow$	$F_\beta^\omega \uparrow$	$F_\beta \uparrow$	MAE \downarrow			
LAFB	0.957	0.919	0.930	0.027	0.924	0.910	0.919	0.028	0.930	0.882	0.896	0.037	10	453.03	139.73
w/o AFB	0.940	0.885	0.906	0.041	0.911	0.870	0.892	0.043	0.922	0.853	0.884	0.045	12	190.93	27.88
w/o AEM	0.946	0.904	0.920	0.033	0.912	0.885	0.902	0.038	0.926	0.868	0.885	0.041	11	420.78	118.15
w/o IIGM	0.946	0.886	0.915	0.039	0.902	0.868	0.895	0.042	0.927	0.863	0.885	0.040	11	448.28	136.53

TABLE VI

ABLATION STUDIES ON RGBT DATASETS, INCLUDING VT5000 [14] TEST SET, VT1000 [12] DATASET AND VT821 [11] DATASET. *w/o* MEANS TO DISCARD THE CORRESPONDING COMPONENT. THE BEST RESULTS ARE MARKED WITH **BOLD**. AFB: ADAPTIVE FUSION BANK, AEM: ADAPTIVE ENSEMBLE MODULE, AND IIGM: INDIRECT INTERACTIVE GUIDANCE MODULE

Models	VT5000 [14]				VT1000 [12]				VT821 [11]				FPS \uparrow	parameters(M) \downarrow	GFLOPs \downarrow
	$E_\xi \uparrow$	$F_\beta^\omega \uparrow$	$F_\beta \uparrow$	MAE \downarrow	$E_\xi \uparrow$	$F_\beta^\omega \uparrow$	$F_\beta \uparrow$	MAE \downarrow	$E_\xi \uparrow$	$F_\beta^\omega \uparrow$	$F_\beta \uparrow$	MAE \downarrow			
LAFB	0.931	0.841	0.857	0.030	0.945	0.905	0.905	0.018	0.915	0.817	0.843	0.034	7	453.03	139.73
w/o AFB	0.904	0.799	0.815	0.041	0.931	0.880	0.882	0.026	0.885	0.778	0.792	0.046	9	190.93	27.88
w/o AEM	0.917	0.819	0.839	0.036	0.941	0.899	0.899	0.018	0.886	0.783	0.803	0.057	8	420.78	118.15
w/o IIGM	0.912	0.815	0.830	0.037	0.937	0.893	0.893	0.021	0.897	0.792	0.813	0.040	7	448.28	136.53

TABLE VII

PERFORMANCE COMPARISON RESULTS OF MAX F-MEASURE ON 5 CHALLENGES. LI, TC, IC, SV AND CB REPRESENT THE CORRESPONDING CHALLENGE-ANNOTATED DATA IN THE TESTING SET OF VT5000 [14], RESPECTIVELY. *only* MEANS TO COVER THE FUSION BANK WITH ONLY ONE FUSION SCHEME. THE BEST RESULTS ARE MARKED IN **BOLD** AND THE SUB-OPTIMAL RESULTS ARE UNDERLINED

Models	LI	TC	IC	SV	CB
LAFB	0.906	0.900	0.870	0.896	0.897
<i>only Fus^{li}</i>	<u>0.900</u>	0.866	0.835	0.871	0.864
<i>only Fus^{td}</i>	0.889	<u>0.897</u>	0.844	0.869	0.863
<i>only Fus^{ic}</i>	0.869	0.885	<u>0.852</u>	0.878	0.874
<i>only Fus^{sv}</i>	0.892	0.867	0.844	<u>0.886</u>	0.878
<i>only Fus^{cb}</i>	0.886	0.865	0.846	0.882	<u>0.884</u>
LAFB (<i>w/o</i> AFB)	0.875	0.863	0.819	0.857	0.850

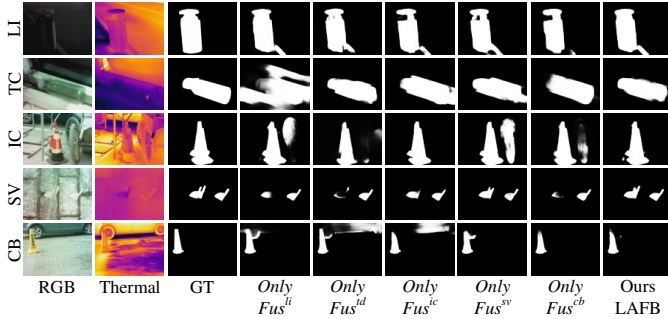


Fig. 8. Visual ablation results for each single fusion scheme on the five challenges. *only*: cover all fusion schemes with the corresponding only one fusion scheme. LI, TC, IC, SV and CB represent the challenges.

scenes in the RGBD SOD dataset.

C. Ablation Study

In order to verify the effectiveness of the main components in our framework, we carry out ablation studies to investigate their importance. The results on RGBD and RGBT datasets are shown in Table V and Table VI, respectively. In these tables, *w/o* means disabling the corresponding components

and LAFB means our proposed complete model. We also explore the effectiveness of each fusion scheme in the adaptive fusion bank, and the results are shown in Table VII. Table IX and Table X present the performance comparison results of different integration strategies for multi-level features and different loss settings, respectively.

1) *Effect of adaptive fusion bank*: To evaluate the effectiveness of our adaptive fusion bank (AFB), we compare the performance of our network with that of removing the AFB, denoted as '*w/o* AFB' in the first row of Table V and Table VI. This means that the features of the two modalities have no interaction for challenges. Specifically, we directly concatenate the multi-modal features in a channel-wise manner and feed them into the following module. Without the AFB, the average values on the four evaluation metrics (E_ξ , F_β^ω , F_β , MAE) drop by 1.3%, 3.6%, 2.3%, 42.4% on the three RGBD test datasets, and 2.6%, 4.2%, 4.4%, 38.8% on the three RGBT test datasets, respectively. Moreover, the results on FPS, parameters and GFLOPs show that the computational complexity of the model without AFB are significantly reduced, because AFB integrates multiple fusion branches, and is embedded into multiple layers.

To verify that each fusion scheme specializes in its corresponding challenges, we evaluate the performance of different fusion schemes on the five challenges in Table VII. Specifically, we cover the entire fusion bank with five fusion schemes sequentially to obtain different models, and then train them successively with the entire training set of VT5000 [14]. Next, we compute the max F-measure score for each model on the five challenges annotated in the testing set of VT5000. The results indicate that each fusion scheme achieves better performance on the challenge that they should address, despite its simple structure. The comparison between these models and our LAFB also demonstrates that our method fully leverage the complementary benefits of these basic fusion schemes to handle different challenges effectively. In the SV column of Table VII, Fus^{cb} performs better than Fus^{ic} . The reasons for

TABLE VIII

PERFORMANCE COMPARISON RESULTS OF DIFFERENT COMBINATIONS OF FUSION SCHEMES ON VT5000 [14] TEST SET FOR THE RGBT MODEL AND NJUD [56] TEST SET FOR THE RGBD MODEL. THE BEST RESULTS ARE MARKED WITH **BOLD**.

Models	Fusion schemes					VT5000 [14]			NJUD [56]		
	F_{us}^{lt}	F_{us}^{td}	F_{us}^{ic}	F_{us}^{sv}	F_{us}^{cb}	$E_{\xi} \uparrow$	$F_{\beta} \uparrow$	$MAE \downarrow$	$E_{\xi} \uparrow$	$F_{\beta} \uparrow$	$MAE \downarrow$
(a)	✓			✓		0.917	0.838	0.035	0.917	0.902	0.038
(b)			✓	✓		0.917	0.839	0.036	0.913	0.898	0.038
(c)	✓	✓	✓			0.920	0.842	0.033	0.915	0.905	0.034
(d)	✓	✓	✓	✓		0.928	0.852	0.031	0.919	0.912	0.031
LAFB	✓	✓	✓	✓	✓	0.931	0.857	0.030	0.924	0.919	0.028

this are as follows: First, in scale variation challenge, multiple objects and large objects can easily cause objects to be off-center, which falls under the center bias (CB) challenge that is handled by F_{us}^{cb} . Second, while the two convolution layers in F_{us}^{ic} bring a higher receptive field, they also lose much local and detailed information, which is preserved by F_{us}^{cb} and is important for accurately recognizing small objects under the scale variation challenge. Fig. 8 vividly illustrates the visual results of the corresponding models in Table VII across different challenge scenes. It can be seen that models with only a single fusion scheme focus on addressing their own challenges, while failing to address all the challenges well at the same time. In contrast, our whole model is able to adaptively exploit the advantages of the corresponding fusion schemes based on different inputs to solve multiple challenges simultaneously.

Furthermore, we perform the experiments with a combination of different fusion schemes, and the results are shown in Table VIII. It can be seen that with more fusion schemes, the model has higher performance, and the whole model (i.e., LAFB) with all five fusion schemes achieves the optimal performance. In addition, compared with the removal of all fusion schemes (i.e., w/o AFB) in Table V and VI, the models with fusion schemes have superior performance on all three metrics (i.e., E_{ξ} , F_{β} , and MAE). This is mainly because models with more fusion schemes can comprehensively deal with different challenges.

2) *Effect of adaptive Ensemble Module*: To verify the effectiveness of AEM, we replace it with channel-wise concatenation, which means that the fusion bank cannot select fusion schemes adaptively. The results are shown in the third row of both Table V and Table VI. Without AEM, the average value of the MAE metric drops by an average of 22.9% on the three RGBD datasets. Comparison with the results of our LAFB illustrates that AEM further improves the performance based on different fusion schemes. This is mainly because AEM enhances the output features of corresponding fusion schemes that can deal with the input challenges.

3) *Effect of indirect interactive guidance module*: To verify the effectiveness of the indirect interactive guidance module (IIGM), we conduct an ablation study by removing the IIGM and feeding the hierarchical outputs of AFB directly into the decoder to generate predictions. The model is denoted as "w/o IIGM" in Table V and Table VI. The results show that IIGM improves the performance of our model on

TABLE IX

PERFORMANCE COMPARISON RESULTS OF DIFFERENT INTEGRATION STRATEGIES OF THE INDIRECT INTERACTIVE GUIDANCE MODULE ON VT5000 [14] TEST SET FOR THE RGBT MODEL AND NJUD [56] TEST SET FOR THE RGBD MODEL. THE BEST RESULTS ARE MARKED WITH **BOLD**. TOP-DOWN: INTEGRATING FEATURES LAYER BY LAYER, AND DIRECT: INTEGRATING ALL FOUR-LAYER FEATURES

Models		VT5000 [14]			NJUD [56]		
		$E_{\xi} \uparrow$	$F_{\beta} \uparrow$	$MAE \downarrow$	$E_{\xi} \uparrow$	$F_{\beta} \uparrow$	$MAE \downarrow$
LAFB		0.931	0.857	0.030	0.924	0.919	0.028
Top-down	(a)	0.918	0.835	0.034	0.910	0.905	0.037
	(b) [2]	0.920	0.843	0.035	0.911	0.905	0.034
	(c) [29]	0.922	0.848	0.033	0.915	0.906	0.035
Direct	(d)	0.926	0.852	0.032	0.922	0.915	0.031
	(e) [33]	0.924	0.845	0.031	0.917	0.913	0.032
	(f) [28]	0.923	0.845	0.032	0.923	0.910	0.032
	Ours LAFB						

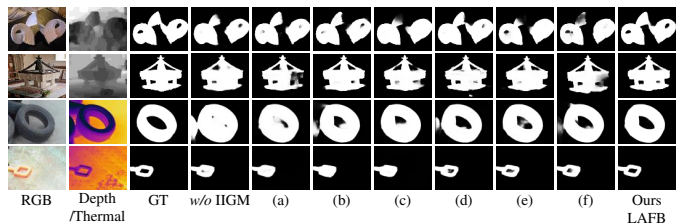


Fig. 9. Saliency maps for different integration approaches of multi-level features. w/o IIGM: removing IIGM in the network, Direct integration: integrating two-layer features, and Full integration: integrating all four-layer features.

all evaluation metrics through the indirect integration and guidance of multi-level features. Without IIGM, the average value on MAE metric drops by an average of 34.2% on the three RGBD datasets. Furthermore, the impact of IIGM on the computational complexity is negligible, as shown in the results on FPS, parameters, and GFLOPs.

Moreover, we conduct experiments to compare the IIGM with top-down and direct integration in Table IX. For the top-down integration, we first directly fuse features layer by layer through a convolutional block, with the results reported in Table IX (a). To further validate the effectiveness of the IIGM, we replace the IIGM with other top-down integration methods [2], [29], and the results are shown in Table IX (b) and (c). By comparing these methods with the first row (i.e., LAFB) in Table IX, we observe that the top-down integration has lower performance on all evaluation metrics. The limited number of adjacent layers restricts the diversity of features and prevents the full integration of multi-level features. For direct integration, we first fuse all four-layer features directly, with the results shown in Table IX (d). In addition, we also replace the IIGM with other direct integration methods [28], [33], the results are denoted as (e) and (f) shown in Table IX. These direct integration methods neglect the differences between high-level and low-level features and mix all features without specific guidance, resulting in sub-optimal performance. Nonetheless, integrating multi-layer features in Table IX all yield better results than "w/o IIGM" in Table V and Table VI, proving that multi-layer fusion can aid in accurately detecting salient regions. Fig. 9 also illustrates the saliency maps for several representative examples of hollow objects. Our method

TABLE X
PERFORMANCE COMPARISON RESULTS OF DIFFERENT LOSS SETTINGS ON VT5000 [14] TEST SET FOR THE RGBT MODEL AND NJUD [56] TEST SET FOR THE RGBD MODEL. THE BEST RESULTS ARE MARKED WITH **BOLD**. λ_i , ℓ_s AND ℓ_d REPRESENT WEIGHTS PARAMETERS, SMOOTHNESS LOSS AND DICE LOSS, RESPECTIVELY

Models	Loss settings						VT5000 [14]			NJUD [56]		
	λ_2	λ_3	λ_4	λ_5	ℓ_s	ℓ_d	$E_{\xi} \uparrow$	$F_{\beta} \uparrow$	$MAE \downarrow$	$E_{\xi} \uparrow$	$F_{\beta} \uparrow$	$MAE \downarrow$
LAFB	1.0	0.8	0.6	0.5	✓	✓	0.931	0.857	0.030	0.924	0.919	0.028
(a)	1.0	1.0	1.0	1.0	✓	✓	0.920	0.845	0.033	0.920	0.910	0.033
(b)	1.0	0.0	0.0	0.0	✓	✓	0.928	0.850	0.032	0.918	0.906	0.037
(c)	1.0	0.8	0.6	0.5	✓		0.925	0.842	0.032	0.920	0.908	0.033
(d)	1.0	0.8	0.6	0.5	✓		0.922	0.846	0.033	0.920	0.908	0.033
(e)	1.0	0.8	0.6	0.5			0.914	0.837	0.036	0.910	0.894	0.037

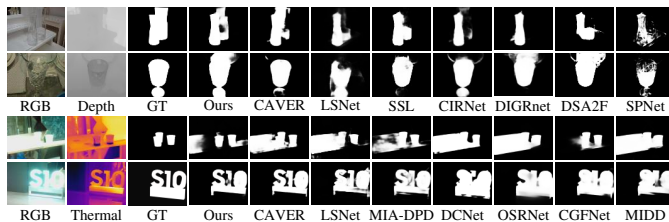


Fig. 10. Visual results of some typical failure cases from RGBD and RGBT testing datasets.

accurately locates the salient regions while suppressing the non-salient regions in the objects. For example, in the first and second rows of Fig. 9, although the hollowed-out background area is small, our method is still able to suppress it. This is because our IIGM can fully integrate semantic and detailed information in multi-level features.

4) *Effect of loss function*: Our total loss (i.e., ℓ_{total}) consists of the main loss (i.e., ℓ_2 , ℓ_s and ℓ_d) and the auxiliary loss (i.e., ℓ_3 , ℓ_4 and ℓ_5). The main loss is used to constrain the final saliency map S_2 , and the auxiliary loss is used to constrain the intermediate features of the decoder to learn discriminative information for saliency detection. We set the weight parameters of the main loss to the default value of 1.0 to emphasize its dominance. The weight parameters (i.e., λ_3 , λ_4 and λ_5) in the auxiliary loss are set to 0.8, 0.6 and 0.5 in a decreasing manner to gradually weaken the impact of the intermediate features.

To demonstrate the effectiveness of the auxiliary loss, we first set the weight parameters (i.e., λ_3 , λ_4 and λ_5) to 1.0, treating all losses equally. As shown in Table X, the comparison between this setting and our LAFB confirms the importance of discriminative treatment of the auxiliary loss. Additionally, we disable the auxiliary loss by setting its weight parameters to 0. Comparing the results in Table X (b) with our LAFB, we observe that removing the auxiliary loss degrades the performance. Furthermore, comparing the results in (a) and (b) shows that the equal treatment of the auxiliary loss can have negative effects.

In order to verify the role of smoothness loss (i.e., ℓ_s) and dice loss (i.e., ℓ_d) in the main loss, we remove them successively. The results are shown in (c) and (d) of Table X, respectively. It can be seen that the smoothness loss and the dice loss play an important role in optimizing the model.

Furthermore, we remove the smoothness loss and the dice loss simultaneously to observe their joint effectiveness. As shown in (e) of Table X, the average index of three metrics (E_{ξ} , F_{β} , MAE) on the two testing datasets decrease by 1.7%, 2.6% and 26.1%, respectively. It indicates that using both ℓ_s and ℓ_d works better than using one of them alone.

D. Failure Cases and Analyses

Although our method is able to address the main challenges in multi-modal SOD, there are still some failure cases, as shown in Fig. 10. For the samples in the first and second rows, the salient objects are transparent, leading to a lack of visible color and texture information in the RGB modality. In this case, our model and other models struggle to accurately locate the salient region and tend to introduce noise from the background and depth map. For the samples in the third and fourth rows, overexposure causes both our model and the existing state-of-the-art ones to focus more on the exposed area, which makes it difficult to distinguish foreground and background areas. These issues remain to be resolved, and we will attempt to design a common fusion scheme to deal with the remaining challenges in future work.

V. CONCLUSION

In this paper, we propose to learn an adaptive fusion bank (LAFB) for robust multi-modal salient object detection (MSOD). Considering the characteristics of different challenges, we design a fusion bank comprising five fusion schemes for the five main challenges in MSOD. In order to further form the adaptive fusion bank (AFB), we introduce an adaptive ensemble module (AEM), which takes advantage of the complementarity of the fusion schemes. In addition, the proposed indirect interactive guidance module (IIGM) improves the prediction for hollow objects in MSOD by fully integrating high-level semantic and low-level detailed features. Experimental results on multiple multi-modal datasets prove the superiority of our LAFB and the effectiveness of the proposed modules.

Although this paper addresses the main and important challenges in MSOD, there are still some difficult challenges to be addressed, such as occlusion, blur, etc. In the future, we will consider developing a common fusion scheme to deal with the remaining challenges and integrate it with the existing AFB to handle the challenges in MSOD more comprehensively.

REFERENCES

- [1] J. Wang, K. Song, Y. Bao, L. Huang, and Y. Yan, "Cgfnet: Cross-guided fusion network for rgb-t salient object detection," *IEEE Transactions on Circuits and Systems for Video Technology*, vol. 32, no. 5, pp. 2949–2961, 2021.
- [2] T. Zhou, H. Fu, G. Chen, Y. Zhou, D.-P. Fan, and L. Shao, "Specificity-preserving rgb-d saliency detection," in *Proceedings of the IEEE/CVF International Conference on Computer Vision*, 2021, pp. 4681–4691.
- [3] W. Wang, J. Shen, R. Yang, and F. Porikli, "Saliency-aware video object segmentation," *IEEE transactions on pattern analysis and machine intelligence*, vol. 40, no. 1, pp. 20–33, 2017.
- [4] W. Wang, G. Sun, and L. Van Gool, "Looking beyond single images for weakly supervised semantic segmentation learning," *IEEE Transactions on Pattern Analysis and Machine Intelligence*, 2022.

- [5] W. Wang, J. Shen, and H. Ling, "A deep network solution for attention and aesthetics aware photo cropping," *IEEE transactions on pattern analysis and machine intelligence*, vol. 41, no. 7, pp. 1531–1544, 2018.
- [6] X. Zheng, X. Tan, J. Zhou, L. Ma, and R. W. Lau, "Weakly-supervised saliency detection via salient object subitizing," *IEEE Transactions on Circuits and Systems for Video Technology*, vol. 31, no. 11, pp. 4370–4380, 2021.
- [7] R. Cong, Q. Qin, C. Zhang, Q. Jiang, S. Wang, Y. Zhao, and S. Kwong, "A weakly supervised learning framework for salient object detection via hybrid labels," *IEEE Transactions on Circuits and Systems for Video Technology*, vol. 33, no. 2, pp. 534–548, 2022.
- [8] L. Zhu, J. Chen, X. Hu, C.-W. Fu, X. Xu, J. Qin, and P.-A. Heng, "Aggregating attentional dilated features for salient object detection," *IEEE Transactions on Circuits and Systems for Video Technology*, vol. 30, no. 10, pp. 3358–3371, 2019.
- [9] L. Zhang, Q. Zhang, and R. Zhao, "Progressive dual-attention residual network for salient object detection," *IEEE Transactions on Circuits and Systems for Video Technology*, vol. 32, no. 9, pp. 5902–5915, 2022.
- [10] G. Wang, C. Li, Y. Ma, A. Zheng, J. Tang, and B. Luo, "Rgb-t saliency detection benchmark: Dataset, baselines, analysis and a novel approach," in *Chinese Conference on Image and Graphics Technologies*. Springer, 2018, pp. 359–369.
- [11] J. Tang, D. Fan, X. Wang, Z. Tu, and C. Li, "Rgbd salient object detection: benchmark and a novel cooperative ranking approach," *IEEE Transactions on Circuits and Systems for Video Technology*, vol. 30, no. 12, pp. 4421–4433, 2019.
- [12] Z. Tu, T. Xia, C. Li, X. Wang, Y. Ma, and J. Tang, "Rgb-t image saliency detection via collaborative graph learning," *IEEE Transactions on Multimedia*, vol. 22, no. 1, pp. 160–173, 2019.
- [13] Q. Zhang, N. Huang, L. Yao, D. Zhang, C. Shan, and J. Han, "Rgbd-t salient object detection via fusing multi-level cnn features," *IEEE Transactions on Image Processing*, vol. 29, pp. 3321–3335, 2019.
- [14] Z. Tu, Y. Ma, Z. Li, C. Li, J. Xu, and Y. Liu, "Rgbd salient object detection: A large-scale dataset and benchmark," *arXiv preprint arXiv:2007.03262*, 2020.
- [15] A. Li, Y. Mao, J. Zhang, and Y. Dai, "Mutual information regularization for weakly-supervised rgb-d salient object detection," *IEEE Transactions on Circuits and Systems for Video Technology*, 2023.
- [16] B. Tang, Z. Liu, Y. Tan, and Q. He, "Hrtransnet: Hrformer-driven two-modality salient object detection," *IEEE Transactions on Circuits and Systems for Video Technology*, vol. 33, no. 2, pp. 728–742, 2023.
- [17] G. Chen, F. Shao, X. Chai, H. Chen, Q. Jiang, X. Meng, and Y.-S. Ho, "Modality-induced transfer-fusion network for rgb-d and rgb-t salient object detection," *IEEE Transactions on Circuits and Systems for Video Technology*, vol. 33, no. 4, pp. 1787–1801, 2022.
- [18] Q. Zhang, T. Xiao, N. Huang, D. Zhang, and J. Han, "Revisiting feature fusion for rgb-t salient object detection," *IEEE Transactions on Circuits and Systems for Video Technology*, vol. 31, no. 5, pp. 1804–1818, 2020.
- [19] F. Huo, X. Zhu, L. Zhang, Q. Liu, and Y. Shu, "Efficient context-guided stacked refinement network for rgb-t salient object detection," *IEEE Transactions on Circuits and Systems for Video Technology*, vol. 32, no. 5, pp. 3111–3124, 2021.
- [20] L. Qu, S. He, J. Zhang, J. Tian, Y. Tang, and Q. Yang, "Rgbd salient object detection via deep fusion," *IEEE transactions on image processing*, vol. 26, no. 5, pp. 2274–2285, 2017.
- [21] J. Zhang, D.-P. Fan, Y. Dai, S. Anwar, F. Saleh, S. Aliakbarian, and N. Barnes, "Uncertainty inspired rgb-d saliency detection," *IEEE transactions on pattern analysis and machine intelligence*, vol. 44, no. 9, pp. 5761–5779, 2021.
- [22] G. Liao, W. Gao, G. Li, J. Wang, and S. Kwong, "Cross-collaborative fusion-encoder network for robust rgb-thermal salient object detection," *IEEE Transactions on Circuits and Systems for Video Technology*, 2022.
- [23] W. Zhou, Q. Guo, J. Lei, L. Yu, and J.-N. Hwang, "Eccfnnet: Effective and consistent feature fusion network for rgb-t salient object detection," *IEEE Transactions on Circuits and Systems for Video Technology*, vol. 32, no. 3, pp. 1224–1235, 2021.
- [24] J.-X. Zhao, Y. Cao, D.-P. Fan, M.-M. Cheng, X.-Y. Li, and L. Zhang, "Contrast prior and fluid pyramid integration for rgbd salient object detection," in *Proceedings of the IEEE/CVF Conference on Computer Vision and Pattern Recognition*, 2019, pp. 3927–3936.
- [25] Y. Piao, W. Ji, J. Li, M. Zhang, and H. Lu, "Depth-induced multi-scale recurrent attention network for saliency detection," in *Proceedings of the IEEE/CVF International Conference on Computer Vision*, 2019, pp. 7254–7263.
- [26] D.-P. Fan, Z. Lin, Z. Zhang, M. Zhu, and M.-M. Cheng, "Rethinking rgb-d salient object detection: Models, data sets, and large-scale benchmarks," *IEEE Transactions on neural networks and learning systems*, vol. 32, no. 5, pp. 2075–2089, 2020.
- [27] G. Li, Z. Liu, M. Chen, Z. Bai, W. Lin, and H. Ling, "Hierarchical alternate interaction network for rgb-d salient object detection," *IEEE Transactions on Image Processing*, vol. 30, pp. 3528–3542, 2021.
- [28] P. Sun, W. Zhang, H. Wang, S. Li, and X. Li, "Deep rgb-d saliency detection with depth-sensitive attention and automatic multi-modal fusion," 2021.
- [29] W. Ji, J. Li, S. Yu, M. Zhang, Y. Piao, S. Yao, Q. Bi, K. Ma, Y. Zheng, H. Lu, and L. Cheng, "Calibrated rgb-d salient object detection," in *Proceedings of the IEEE/CVF Conference on Computer Vision and Pattern Recognition (CVPR)*, June 2021, pp. 9471–9481.
- [30] N. Liu, N. Zhang, K. Wan, L. Shao, and J. Han, "Visual saliency transformer," in *Proceedings of the IEEE/CVF international conference on computer vision*, 2021, pp. 4722–4732.
- [31] W. Zhou, Y. Zhu, J. Lei, J. Wan, and L. Yu, "Ccafnet: Crossflow and cross-scale adaptive fusion network for detecting salient objects in rgb-d images," *IEEE Transactions on Multimedia*, 2021.
- [32] S. Mohammadi, M. Noori, A. Bahri, S. G. Majelan, and M. Havaei, "Cagnet: Content-aware guidance for salient object detection," *Pattern Recognition*, vol. 103, p. 107303, 2020.
- [33] M. Zhang, Y. Zhang, Y. Piao, B. Hu, and H. Lu, "Feature reintegration over differential treatment: A top-down and adaptive fusion network for rgb-d salient object detection," in *Proceedings of the 28th ACM International Conference on Multimedia*, 2020, pp. 4107–4115.
- [34] S. Woo, J. Park, J.-Y. Lee, and I. S. Kweon, "Cbam: Convolutional block attention module," in *Proceedings of the European conference on computer vision (ECCV)*, 2018, pp. 3–19.
- [35] J. Hu, L. Shen, and G. Sun, "Squeeze-and-excitation networks," in *Proceedings of the IEEE conference on computer vision and pattern recognition*, 2018, pp. 7132–7141.
- [36] Z. Tu, Z. Li, C. Li, Y. Lang, and J. Tang, "Multi-interactive dual-decoder for rgb-thermal salient object detection," *IEEE Transactions on Image Processing*, 2021.
- [37] Z. Tu, Z. Li, C. Li, and J. Tang, "Weakly alignment-free rgbd salient object detection with deep correlation network," *IEEE Transactions on Image Processing*, 2022.
- [38] H. Chen and Y. Li, "Progressively complementarity-aware fusion network for rgb-d salient object detection," in *Proceedings of the IEEE conference on computer vision and pattern recognition*, 2018, pp. 3051–3060.
- [39] K. Fu, D.-P. Fan, G.-P. Ji, and Q. Zhao, "Jl-dcf: Joint learning and densely-cooperative fusion framework for rgb-d salient object detection," in *Proceedings of the IEEE/CVF conference on computer vision and pattern recognition*, 2020, pp. 3052–3062.
- [40] N. Liu, N. Zhang, and J. Han, "Learning selective self-mutual attention for rgb-d saliency detection," in *Proceedings of the IEEE/CVF Conference on Computer Vision and Pattern Recognition*, 2020, pp. 13 756–13 765.
- [41] W. Ji, G. Yan, J. Li, Y. Piao, S. Yao, M. Zhang, L. Cheng, and H. Lu, "Dmra: Depth-induced multi-scale recurrent attention network for rgb-d saliency detection," *IEEE Transactions on Image Processing*, vol. 31, pp. 2321–2336, 2022.
- [42] N. Zhang, J. Han, and N. Liu, "Learning implicit class knowledge for rgb-d co-salient object detection with transformers," *IEEE Transactions on Image Processing*, vol. 31, pp. 4556–4570, 2022.
- [43] Y. Pang, X. Zhao, L. Zhang, and H. Lu, "Caver: Cross-modal view-mixed transformer for bi-modal salient object detection," *IEEE Transactions on Image Processing*, 2023.
- [44] Z. Liu, Y. Tan, Q. He, and Y. Xiao, "Swinnet: Swin transformer drives edge-aware rgb-d and rgb-t salient object detection," *IEEE Transactions on Circuits and Systems for Video Technology*, vol. 32, no. 7, pp. 4486–4497, 2022.
- [45] S.-H. Gao, M.-M. Cheng, K. Zhao, X.-Y. Zhang, M.-H. Yang, and P. Torr, "Res2net: A new multi-scale backbone architecture," *IEEE transactions on pattern analysis and machine intelligence*, vol. 43, no. 2, pp. 652–662, 2019.
- [46] N. Huang, Y. Yang, D. Zhang, Q. Zhang, and J. Han, "Employing bilinear fusion and saliency prior information for rgb-d salient object detection," *IEEE Transactions on Multimedia*, 2021.
- [47] O. Ronneberger, P. Fischer, and T. Brox, "U-net: Convolutional networks for biomedical image segmentation," in *International Conference on Medical image computing and computer-assisted intervention*. Springer, 2015, pp. 234–241.
- [48] Z. Wu, L. Su, and Q. Huang, "Cascaded partial decoder for fast and accurate salient object detection," in *Proceedings of the IEEE/CVF*

- Conference on Computer Vision and Pattern Recognition*, 2019, pp. 3907–3916.
- [49] Y.-H. Wu, Y. Liu, J. Xu, J.-W. Bian, Y.-C. Gu, and M.-M. Cheng, “Mobilesal: Extremely efficient rgb-d salient object detection,” *IEEE Transactions on Pattern Analysis and Machine Intelligence*, 2021.
- [50] C. Godard, O. Mac Aodha, and G. J. Brostow, “Unsupervised monocular depth estimation with left-right consistency,” in *Proceedings of the IEEE conference on computer vision and pattern recognition*, 2017, pp. 270–279.
- [51] F. Milletari, N. Navab, and S.-A. Ahmadi, “V-net: Fully convolutional neural networks for volumetric medical image segmentation,” in *2016 fourth international conference on 3D vision (3DV)*. IEEE, 2016, pp. 565–571.
- [52] C. Zhu and G. Li, “A three-pathway psychobiological framework of salient object detection using stereoscopic technology,” in *Proceedings of the IEEE International Conference on Computer Vision Workshops*, 2017, pp. 3008–3014.
- [53] Y. Niu, Y. Geng, X. Li, and F. Liu, “Leveraging stereopsis for saliency analysis,” in *2012 IEEE Conference on Computer Vision and Pattern Recognition*. IEEE, 2012, pp. 454–461.
- [54] N. Liu, N. Zhang, L. Shao, and J. Han, “Learning selective mutual attention and contrast for rgb-d saliency detection,” *IEEE Transactions on Pattern Analysis and Machine Intelligence*, vol. 44, no. 12, pp. 9026–9042, 2021.
- [55] H. Peng, B. Li, W. Xiong, W. Hu, and R. Ji, “Rgbd salient object detection: a benchmark and algorithms,” in *European conference on computer vision*. Springer, 2014, pp. 92–109.
- [56] R. Ju, L. Ge, W. Geng, T. Ren, and G. Wu, “Depth saliency based on anisotropic center-surround difference,” in *2014 IEEE international conference on image processing (ICIP)*. IEEE, 2014, pp. 1115–1119.
- [57] Y. Pang, L. Zhang, X. Zhao, and H. Lu, “Hierarchical dynamic filtering network for rgb-d salient object detection,” 2020.
- [58] W. Ji, J. Li, M. Zhang, Y. Piao, and H. Lu, “Accurate rgb-d salient object detection via collaborative learning,” in *Computer Vision—ECCV 2020: 16th European Conference, Glasgow, UK, August 23–28, 2020, Proceedings, Part XVIII 16*. Springer, 2020, pp. 52–69.
- [59] W.-D. Jin, J. Xu, Q. Han, Y. Zhang, and M.-M. Cheng, “Cdnnet: Complementary depth network for rgb-d salient object detection,” *IEEE Transactions on Image Processing*, vol. 30, pp. 3376–3390, 2021.
- [60] W. Zhang, G.-P. Ji, Z. Wang, K. Fu, and Q. Zhao, “Depth quality-inspired feature manipulation for efficient rgb-d salient object detection,” in *Proceedings of the 29th ACM International Conference on Multimedia*, 2021, pp. 731–740.
- [61] Q. Chen, Z. Liu, Y. Zhang, K. Fu, Q. Zhao, and H. Du, “Rgb-d salient object detection via 3d convolutional neural networks,” in *Proceedings of the AAAI Conference on Artificial Intelligence*, vol. 35, no. 2, 2021, pp. 1063–1071.
- [62] X. Zhao, Y. Pang, L. Zhang, H. Lu, and X. Ruan, “Self-supervised pretraining for rgb-d salient object detection,” in *AAAI Conference on Artificial Intelligence*, vol. 3, 2022.
- [63] X. Cheng, X. Zheng, J. Pei, H. Tang, Z. Lyu, and C. Chen, “Depth-induced gap-reducing network for rgb-d salient object detection: An interaction, guidance and refinement approach,” *IEEE Transactions on Multimedia*, 2022.
- [64] R. Cong, Q. Lin, C. Zhang, C. Li, X. Cao, Q. Huang, and Y. Zhao, “Cinnet: Cross-modality interaction and refinement for rgb-d salient object detection,” *IEEE Transactions on Image Processing*, vol. 31, pp. 6800–6815, 2022.
- [65] X. Jin, K. Yi, and J. Xu, “Moadnet: Mobile asymmetric dual-stream networks for real-time and lightweight rgb-d salient object detection,” *IEEE Transactions on Circuits and Systems for Video Technology*, vol. 32, no. 11, pp. 7632–7645, 2022.
- [66] W. Zhou, Y. Zhu, J. Lei, R. Yang, and L. Yu, “Lsnet: Lightweight spatial boosting network for detecting salient objects in rgb-thermal images,” *IEEE Transactions on Image Processing*, vol. 32, pp. 1329–1340, 2023.
- [67] Z. Tu, T. Xia, C. Li, Y. Lu, and J. Tang, “M3s-nir: Multi-modal multi-scale noise-insensitive ranking for rgb-t saliency detection,” in *2019 IEEE Conference on Multimedia Information Processing and Retrieval (MIPR)*. IEEE, 2019, pp. 141–146.
- [68] W. Gao, G. Liao, S. Ma, G. Li, Y. Liang, and W. Lin, “Unified information fusion network for multi-modal rgb-d and rgb-t salient object detection,” *IEEE Transactions on Circuits and Systems for Video Technology*, vol. 32, no. 4, pp. 2091–2106, 2021.
- [69] Y. Liang, G. Qin, M. Sun, J. Qin, J. Yan, and Z. Zhang, “Multi-modal interactive attention and dual progressive decoding network for rgb-d/t salient object detection,” *Neurocomputing*, vol. 490, pp. 132–145, 2022.
- [70] F. Huo, X. Zhu, Q. Zhang, Z. Liu, and W. Yu, “Real-time one-stream semantic-guided refinement network for rgb-thermal salient object detection,” *IEEE Transactions on Instrumentation and Measurement*, 2022.
- [71] P. Sun, W. Zhang, H. Wang, S. Li, and X. Li, “Deep rgb-d saliency detection with depth-sensitive attention and automatic multi-modal fusion,” in *Proceedings of the IEEE/CVF Conference on Computer Vision and Pattern Recognition*, 2021, pp. 1407–1417.
- [72] D.-P. Fan, C. Gong, Y. Cao, B. Ren, M.-M. Cheng, and A. Borji, “Enhanced-alignment measure for binary foreground map evaluation,” *arXiv preprint arXiv:1805.10421*, 2018.
- [73] R. Margolin, L. Zelnik-Manor, and A. Tal, “How to evaluate foreground maps?” in *Proceedings of the IEEE conference on computer vision and pattern recognition*, 2014, pp. 248–255.
- [74] R. Achanta, S. Hemami, F. Estrada, and S. Susstrunk, “Frequency-tuned salient region detection,” in *2009 IEEE conference on computer vision and pattern recognition*. IEEE, 2009, pp. 1597–1604.
- [75] F. Perazzi, P. Krähenbühl, Y. Pritch, and A. Hornung, “Saliency filters: Contrast based filtering for salient region detection,” in *2012 IEEE conference on computer vision and pattern recognition*. IEEE, 2012, pp. 733–740.
- [76] K. He, X. Zhang, S. Ren, and J. Sun, “Deep residual learning for image recognition,” in *Proceedings of the IEEE conference on computer vision and pattern recognition*, 2016, pp. 770–778.
- [77] M. Sandler, A. Howard, M. Zhu, A. Zhmoginov, and L.-C. Chen, “Mobilenetv2: Inverted residuals and linear bottlenecks,” in *Proceedings of the IEEE conference on computer vision and pattern recognition*, 2018, pp. 4510–4520.
- [78] A. Howard, M. Sandler, G. Chu, L.-C. Chen, B. Chen, M. Tan, W. Wang, Y. Zhu, R. Pang, V. Vasudevan *et al.*, “Searching for mobilenetv3,” in *Proceedings of the IEEE/CVF international conference on computer vision*, 2019, pp. 1314–1324.
- [79] K. Simonyan and A. Zisserman, “Very deep convolutional networks for large-scale image recognition,” *arXiv*, 2014.
- [80] Z. Liu, Y. Lin, Y. Cao, H. Hu, Y. Wei, Z. Zhang, S. Lin, and B. Guo, “Swin transformer: Hierarchical vision transformer using shifted windows,” in *Proceedings of the IEEE/CVF international conference on computer vision*, 2021, pp. 10012–10022.